UNIVERSITY OF SOUTHAMPTON

The Synthesis and Structure of Transition Metal Oxides for Battery Applications

A dissertation submitted for the degree of
Master of Philosophy

by

Matthew James Oliver

Department of Chemistry
Southampton

November 2002

UNIVERSITY OF SOUTHAMPTON

ABSTRACT

FACULTY OF SCIENCE
CHEMISTRY

Master of Philosophy

The Synthesis and Structure of Transition Metal Oxides for Battery Applications

by Matthew James Oliver

Low temperature hydrothermal routes to bismuth (V) containing materials have been investigated. Results indicate that $MgBi_2O_6$, obtained by the hydrothermal reaction of magnesium chloride with sodium bismuthate, crystallises with a trirutile-type structure. Attempts to synthesise the equivalent calcium compound yielded $Ca_2Bi_2O_7$, which was found to adopt a pyrochlore structure. The attempted synthesis of the strontium equivalent produced a material with an X-ray diffraction pattern indicative of a layered material with an inter-layer separation of 13.657(4)Å. Single phase products were not obtained under a wide variety of reaction conditions in the case of Zn, Cd, and Ba.

Two new alkali metal iron oxide materials have been synthesised, $RbFeO_2$ and $CsFeO_2$. The structures of these two compounds have been investigated using powder X-ray diffraction and time of flight powder neutron diffraction. Powder neutron data confirmed an orthorhombic space group, Pbca, for $KFeO_2$ and $RbFeO_2$ and a cubic space group, Fd-3m, for $CsFeO_2$. The increased symmetry, as a result of incorporating the larger cations into the structure, is reflected by an opening up of the Fe-O-Fe bond angle from 136.1° ($KFeO_2$) to 151.69° ($RbFeO_2$) and 180° ($CsFeO_2$). Preliminary attempts at exchanging the potassium ion for lithium in these structures were inconclusive but energy dispersive X-ray analysis and ion-conduction data from related compounds indicate that this may be feasible.

Hydrothermal reactions at high-pressures (up to 40000psi) and high temperatures (700°C) were utilised to try and synthesise structures containing manganese stabilised in unusually high oxidation states. The potassium equivalent of the mixed valent $Na_2Mn_3O_7$ could not be formed, X-ray diffraction data pointing to the formation of $K_{1.33}Mn_8O_{16}$ with the hollandite structure.

ACKNOWLEDGEMENTS

Sincere thanks to Bob, Craig, Kenny, Lee, Jon, Paul and Vince.

1 Introduction

1.1 FUTURE DEMANDS ON BATTERIES

Whilst the current uses of primary batteries are many and varied, demand for them, whilst continuing to experience healthy growth, is decelerating relative to previous years. Most demand stems from buying replacements for battery powered devices[i]. Battery companies therefore, are always interested in new battery materials, which may, through advances in their energy density and longevity, be used in an expanding range of applications thereby opening up new markets. Primary batteries are in some cases achieving such advances in performance that they can now be used in applications that were previously the domain of rechargeable batteries. In addition developments in primary cell materials may be transposed to secondary cells, and vice versa. Secondary cells have many applications at the forefront of technology and may enable developments such as electric and hybrid electric vehicles to become a realistic proposition. 900 million lithium ion cells were sold in the year 2000, and it is predicted that production is set to double each year. Furthermore market researchers have identified that consumers are increasingly willing to pay more for improved performance and this has stimulated research.
A growing worldwide emphasis on developing advanced, clean, efficient methods of generating and storing energy as part of the drive towards so called "sustainable development" will also lead to governments keen to fund research in this and related areas as a way of evidencing their green credentials.

1.2 SOLID STATE CHEMISTRY AND NEW BATTERY MATERIALS

1.2.1 Structure-property relationships

There are certain features that are desirable in any material destined for use as a cathode material in an insertion electrode.

- The material must allow lithium to be inserted into the cathode with little detrimental effect on the structure's integrity. This property leads to good reversibility of the material through cycles.
- The material should have a low Fermi level and the lithium ions should have a low potential when located on their host sites in the material. Therefore, for a given *anode* material the difference in the chemical potential of the lithium when sited in the anodic material and its

chemical potential when incorporated into the cathode material is maximised giving the greatest open-circuit voltage.

- The material should be capable of incorporating a large number of Li^+ ions per formula unit as this gives a large energy density. Similarly a low formula mass and low formula volume are desirable.
- The material should not incorporate solvent molecules along with the Li^+ ions and should be stable in contact with the cell electrolyte.
- The electrical conductivity of the material should be high in order to minimise the internal resistance of the cell.
- The material should be cheap and non-toxic.

A knowledge of solid state chemistry and its associated experimental techniques allows us to exercise a degree of control over one or more of the above factors and two of these are discussed in greater detail below. Furthermore these conditions are quite severe and allow us to focus our research onto a refined, but still large, section of materials.

1.2.2 The Fermi Level

The energy of the Fermi level of the cathode material is of particular importance when designing insertion electrodes, and is a factor that can be controlled through solid-state chemistry.

$$V = -\frac{(\mu_{Li^+} + \mu_{e^-})^{cathode} - (\mu_{Li^+} + \mu_{e^-})^{anode}}{nF}$$

Equation 1-1: The equation relating chemical potential to voltage for a lithium cell

In a battery electrons travel through the external circuit performing work and finally combine with the bulk cathode material with an energy equal to that of the Fermi level of the material. Hence, according to Equation 1-1, the sum of chemical potentials of the lithium ions and electrons in the cathode should be low relative to the potentials in the anode, giving the maximum potential difference.

A lot of battery materials in use today are oxide materials, specifically transition metal oxides and a lot of new research is focused on this area. Both of these trends can be explained using energetic arguments.

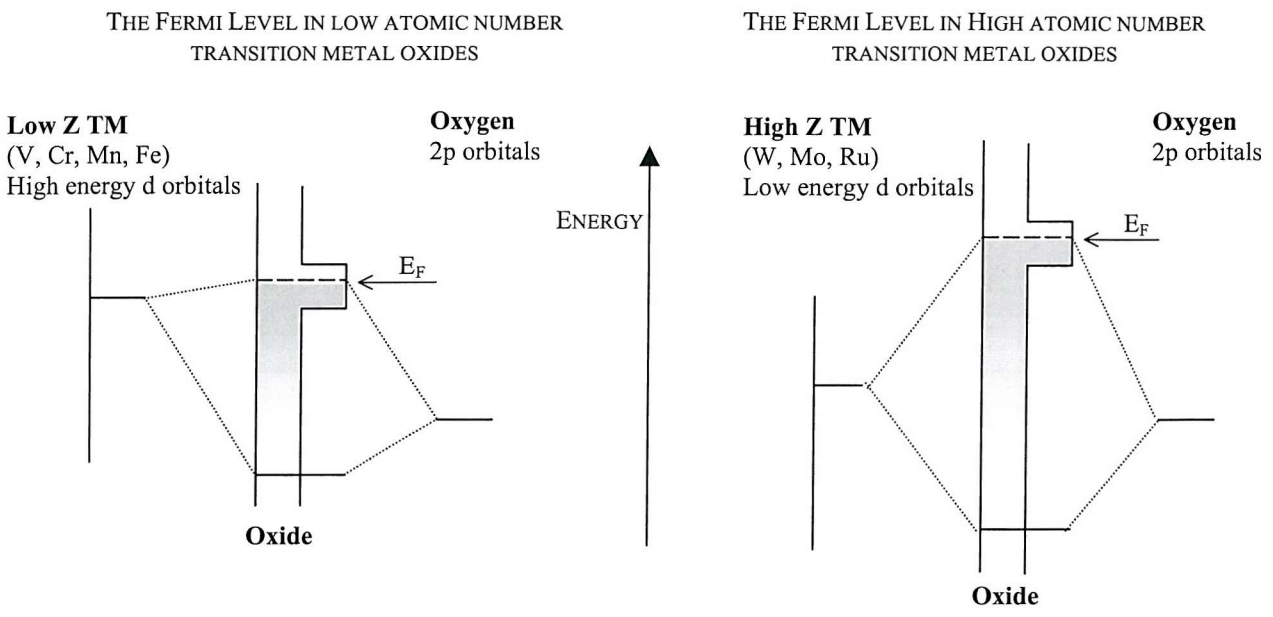

Figure 1-1: A band theory model of the bonding in transition metal oxides

In first row transition metals oxides there tends to be a weak overlap of the low energy oxygen 2p orbital with the high-energy metal d-orbitals. The splitting in the complex is weak and once all the available electrons have been placed in the resultant orbitals they fill up to a level which is only slightly antibonding and therefore low in energy. The corresponding second and third row transition metals have d-orbitals, which are much closer in energy to oxygen p orbitals creating a large splitting. In this case electrons have to occupy highly anti-bonding bands and a high-energy Fermi level results. This explains the preference for early transition metal compounds as cathode materials, they are selected because of their low Fermi levels..

Sulphides have been investigated for use in cells but the valence orbitals of these materials are of 3p character and their energy significantly greater than that of the oxygen 2p-valence orbitals. Hence in sulphides the overlap with transition metal d orbitals is weak and the resulting Fermi energy level is high compared to that of oxide materials. Cells using sulphide materials do not, therefore, give as high a cell voltage as oxides.

1.2.3 Li^+ site energy

Small cations with a full outer core of electrons such as lithium can be considered as spherical and therefore its interaction with surrounding atoms to be unidirectional. Therefore in an

insertion compound consisting of both octahedral and tetrahedral vacancy sites lithium will preferentially occupy the tetrahedral sites due to the more stable distribution of atoms about the lithium compared to the octahedral sites.

This phenomenon can result in large differences in cell potential depending on the geometries of the sites available for lithium insertion. For instance in $LiMn_2O_4$ lithium is coordinated in a tight tetrahedral manner and the electrode potential is 4.1V, whereas octahedral coordination gives a stoichiometry of $Li_2Mn_2O_4$ and an electrode potential of 3V.

1.2.4 The Jahn-Teller Effect

> *"If the ground electronic configuration of a non-linear molecule is degenerate, then the molecule will distort so as to remove the degeneracy and achieve a lower energy."*

This phenomenon is an important factor in determining the amount of distortion that a material's structure will be subjected to during its many oxidation and reduction cycles as a battery material. According to the theory it is possible to predict that in an octahedral environment a Jahn-Teller active ion, will experience a tetragonal distortion corresponding to an extension along the z-axis and a compression along the x and y axes. This serves to remove the degeneracy of the t_{2g} and e_g orbitals and there is an overall stabilisation of the complex.

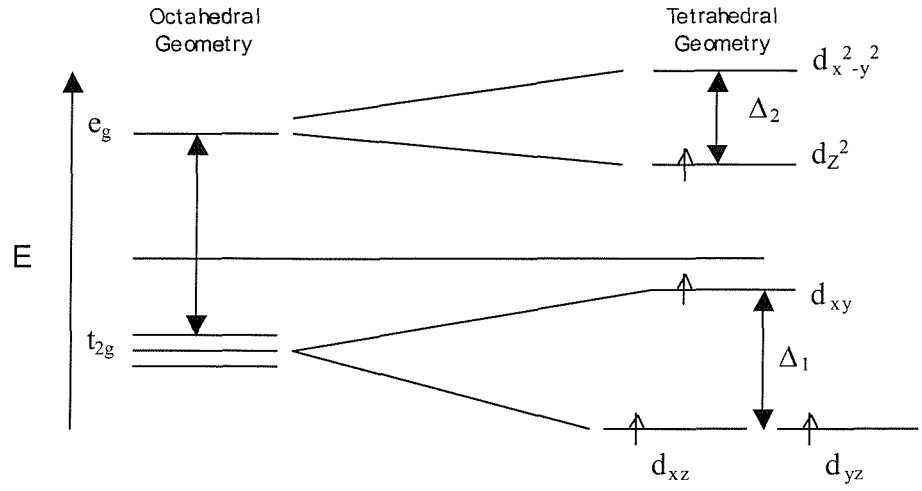

Figure 1-2: The energy level changes upon tetragonal distortion of a d^4 complex such as Mn^{3+}.

1.3 CURRENT BATTERY MATERIALS

1.3.1 First generation lithium cells – $LiCoO_2$

The first revolution in battery design came with the introduction of the Li-ion cell by Sony in 1990, Figure 1-2. This cell consists of a $LiCoO_2$ anode and a graphitic cathode with a lithium salt dissolved in ethylene carbonate as the electrolyte. The cell is able to store three times the amount of energy in a given unit weight and volume[ii], compared to conventional systems and as Bruce states represents "a remarkable achievement in an industry that traditionally measures improvements in a few percentage points". The limiting factor in the performance of this cell is the tolerance of the anode's structure towards the reversible intercalation of lithium. In the case of $LiCoO_2$ half the lithium present may be removed and re-inserted. Instantly the importance of solid-state chemistry in the design of improved anodic materials becomes obvious, as this offers a means of controlling the materials capacity for intercalating lithium.

The changes that occur upon extraction of lithium and oxidation of Co^{3+} to Co^{4+} are interesting and not trivial. Co^{3+} adopts a low spin ($t_{2g}^6 e_g^0$) arrangement in its octahedral environment and the solid is a semi-conductor. The t_{2g} orbitals are very close in energy to the 2p orbitals of oxygen and a strong overlap results with a considerable degree of covalent character. Extraction of lithium results in Co^{4+} (low spin d^5) and the a axis contracts to a distance short enough to allow overlap of the Co^{4+} t_{2g} orbitals across a shared octahedral edge, ie band formation, and metallic behaviour is observed. Ultimately the similar energy of the metal t_{2g} orbitals and the oxygen 2p orbitals leads to the high potential (>4V) of the Co^{4+}/ Co^{3+} couple relative to lithium.

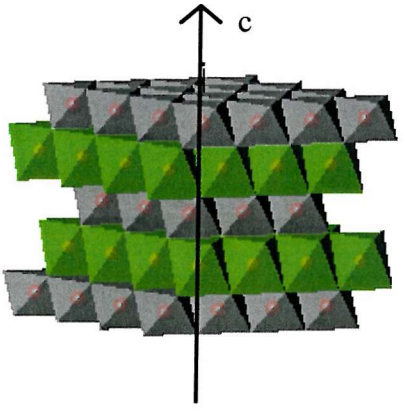

Figure 1-1: $LiCoO_2$ (a=2.82, c=14.08 A) Hexagonal phase with alternating layers of Co (grey) and Li (green) octahedra

Electrode materials such as $LiCoO_2$ are termed insertion electrodes because they operate on the principal of Lithium ions at a high chemical potential in the anode, i.e. in the charged state, *inserting* themselves into the cathode structure upon discharge.

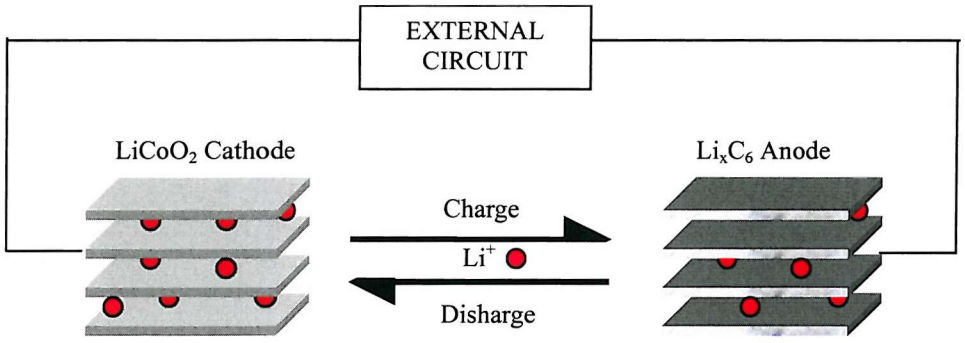

Figure 1-4: The Sony "Rocking chair" cell – a first generation Li-ion cell

1.3.2 Second generation lithium cells

The term second generation is applied to advances in insertion electrode materials since the introduction of the $LiCoO_2$ cell. Advances in the performance of these materials tend to be more modest than the quantum leap in performance associated with the introduction of Sony's rocking chair cell.

As discussed in §1.2.1 when designing alternatives to the $LiCoO_2$ system a number of criteria restrict or direct the choice of potential candidates. Below are outlined three common systems in use today and relevant to this project.

1.3.3 Manganese based cathodes

MnO_2 is a complex compound, with many different polymorphs, categorised using a mixture of "traditional" mineral names and a system that uses a letter of the Greek alphabet as a prefix, Table 1-1 attempts to clarify the situation regarding some of these structures.

Broadly the various forms all consist of MnO_6 octahedral units sharing corners or edges and may be divided into 3 different categories.

- Chemically pure forms with close packed structures whose structure is well characterised. Examples are pyrolusite β-MnO_2 with a rutile type structure, ramsdellite MnO_2 related to the rutile form, and spinel λ-MnO_2.

- Structural forms relating to the mineral nsutite with random oriented domains of the rutile and ramsdellite forms.
- Layered structures of MnO_2

At present most manganese containing cathode materials are those classified as having structures related to nsutite as this is the form most readily produced using electrolytic or chemical synthetic methods. These materials, when synthetically produced, are labeled γ-MnO_2. A review of the properties and characterisation of this form alone reaches 130 pages[iii].

Name	Symmetry	Lattice Parameter/Å	Structure
α-MnO_2 (Hollandite, Cryptomelane)	Tetragonal (I*4/m*)	a = 9.81, c = 2.85	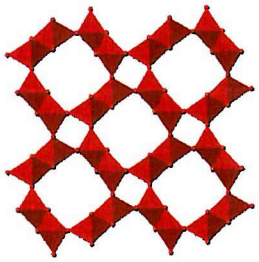
β-MnO_2 Pyrolusite	Tetragonal (P*4/mnm*)	a = 2.39, c = 2.87	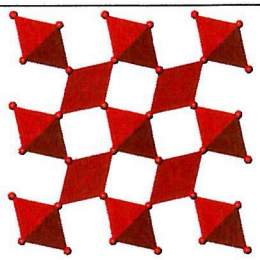
R-MnO_2 (Ramsdellite)	Orthorhombic (P*bnm*)	a = 4.53, b = 9.27 c = 2.87	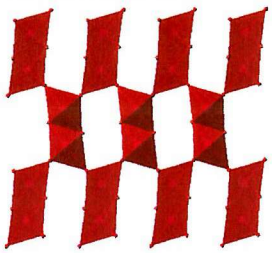
γ-MnO_2 (nsutite)	-	a = 9.65, c = 4.43	Randomly dispersed domains of β-MnO_2 and R-MnO_2.
λ-MnO_2 (Spinel type, e.g. $LiMn_2O_4$)	Cubic (F*d3m*)	a = 8.04	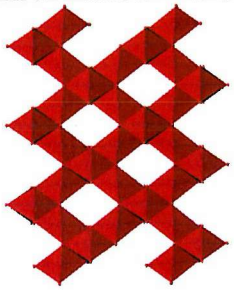
Layered $[MnO_6]^-$ octahedra (e.g. $LiMnO_2$)	Monoclinic (C*2/m*)	a = 2.39, c = 2.87	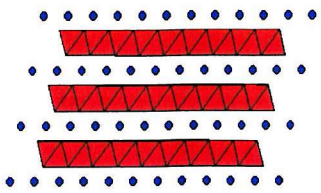

Table 1-1: Some of the forms of MnO_2 used as cathodic materials in cells.

MnO_2 has long been used in *primary* battery materials where it is combined with a zinc anode and a KOH electrolyte, hence the term alkali battery. The cell reactions are as follows;

Anode $\quad Zn \rightarrow Zn^{2+} + 2e^-$

Cathode $\quad MnO_2 + xH^+ + e^- \rightarrow xMn_{(1-x)}OOH$

This technology has been in use for over a century. The improvements made in this technology over that time can still be helpful when trying to design new electrodes, for instance zinc is used in a powdered form at the anode to increase the surface area allowing for more particle interaction. This lowers the internal resistance and increases the power density. Therefore researchers now look to use preparative techniques that generate small particle sizes of material.

It was during the 1960's that NASA and the US military began to investigate using lithium as the anodic material and its ions as charge carriers. The motivation for this work was the fact that lithium is the most electropositive and lightest of all the metallic elements. The use of lithium presented scientists with a number of challenges however, perhaps the most obvious being that all materials used in the cell would have to be anhydrous and the electrolyte non aqueous to prevent a potentially dangerous reaction with the lithium. This improvement at least had the benefit of preventing the gassing and lowering of the oxidation state of Mn in $Mn^{IV}O_2$ during storage that had plagued earlier systems[iv].

It was initially suggested [v] that the cell reaction for the Li/MnO_2 system was

$$2Li + 2MnO_2 \rightarrow Mn_2O_3 + Li_2O$$

however X-ray diffraction experiments by Ikeda et al.[vi] showed that Mn_2O_3 and Li_2O were not present in the discharged state. Furthermore the peaks in the X-Ray pattern showed a shift to lower angles indicating an increase in the lattice parameters indicating incorporation of lithium into the MnO_2 crystal lattice. Thus it was deduced that the Li/MnO_2 cell reaction, in a non-aqueous electrolyte, is likely to be;

$$Li + Mn^{(IV)}O_2 \rightarrow Mn^{(III)}O_2(Li^+)$$

with the Li^+ ion behaving like the proton in the Zn/MnO_2 aqueous system. This mechanism has been confirmed by atomic absorption spectroscopy.

The electrode potential of the half-cell reaction depends on the activity of the oxidised and reduced forms as given by Equation 1-2.

$$V \approx \frac{RT}{F} \ln a_{Li^+}$$
$$V \approx \frac{RT}{F} \ln a_{Li^+} + \frac{RT}{F} \ln a_{e-}$$
$$V \approx \frac{RT}{F} \ln \frac{(1-x)}{x} - E_F$$

Equation 1-2

The open cell voltage, V, for the Li/MnO_2 system is approximately 3V.

The need to intercalate lithium into the MnO_2 structure presents a number of challenges when attempting to construct a secondary, i.e. rechargeable, cell. Insertion of lithium into MnO_2 causes drastic modification of the structure as it accommodates the Li^+ ions[vii,viii]. Irreversible structural damage can occur caused by, amongst other things, the instability of hcp MnO_2 structures as they tend towards ccp upon lithiation, the displacement of manganese ions onto interstitial sites of the host structure, and lattice distortions due to a Jahn-Teller effect as the concentration of Mn^{3+} ions (d^4) increases. A lot of advances in the suitability of MnO_2 as an insertion electrode material have focused on attempts at stabilising the MnO_2 structure to minimise the negative impact of lithium intercalation. Techniques for doing this include doping of the compound with other elements[ix] or reaction with lithium oxide to produce "lithia-stabilised" structures[x].

There is so much interest in manganese based cells because Mn(IV) has a high redox potential, low cost, and is environmentally benign, much more so than some common alternatives such as nickel and cobalt. Some properties of these types of cells are given in Table 1-2. Dry cells manufactured using MnO_2 are cheap and reliable, but suffer from a low energy density (theoretically about 125 Wh/kg but in reality about half this).

Cell Couple	OCV (v)	Energy Density (Wh kg^{-1})	Specific Power (W kg^{-1})	Temp Range (°C)
Li/Li_xCoO_2	4	135	200-250	-20 to 60
Li/MnO_2	3	120-150	76	-40 to 85
Zn/MnO_2(alkaline)	1.5	150	14	-30 to 55

Table 1-2: Comparison of the features of some of the most common battery systems

1.3.4 The Li/Mn_2O_4 System

$LiMn_2O_4$, first investigated as a cathode material in 1983[xi], forms with the spinel structure (Fd3m) and has all the benefits associated with the use of manganese but also desirable structural features that make it an attractive as a cathode insertion material.

$LiMn_2O_4$ is synthesised by heating MnO_2 and the carbonate or nitrate salt of lithium in a platinum or nickel crucible for 12 to 200 hours at temperatures from 450 to 850°C. There is a bewildering array of permutations and combinations of synthesis conditions that can have an effect on the discharge characteristics of the final compound[xii].

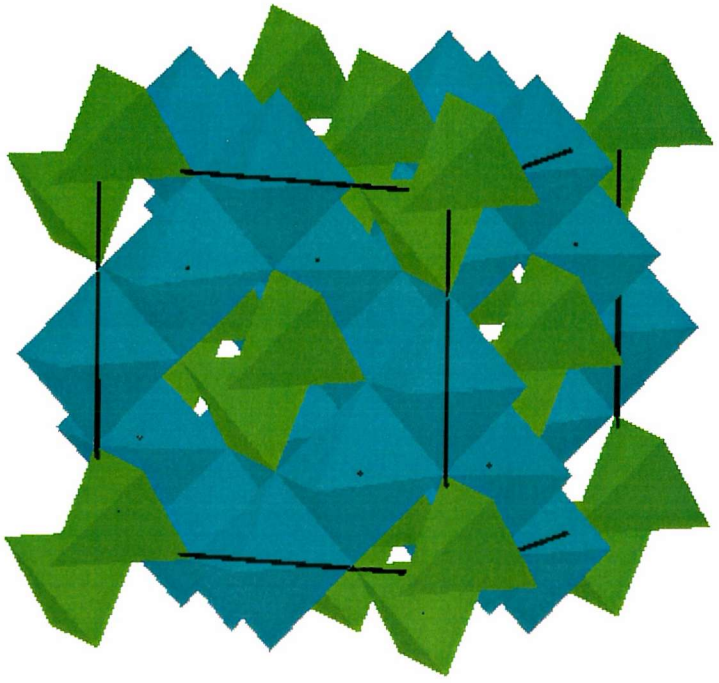

Figure 1-1: The LiMn2O4 spinel unit cell showing the intersecting arrays of Li tetrahedra (green) and Mn octahedra (blue).

The structure, Figure 1-1, can be considered as cubic close-packed oxide ions with manganese ions in half of the octahedral sites and Li^+ in one eighth of the tetrahedral sites within the array. This arrangement creates tunnels defined by the face sharing of tetrahedral lithium and empty octahedral sites. These tunnels intersect the material in three dimensions and facilitate rapid lithium diffusion throughout the structure.

The main problem with this material is the disruption caused to the structure by the transition from the Jahn-Teller active Mn^{3+} to the non Jahn-Teller active, low spin Mn^{4+}. Recently doping of the structure with sulphur has been used to completely overcome this problem and the resulting material also exhibits good cyclability[xiii].

1.3.5 Layered $LiMnO_2$

For a long time researchers attempted to synthesise a manganese analogue of the layered $LiCoO_2$ used in the Sony cell but Li-Mn-O compositions do not readily form into structures of this type, being thermodynamically unstable above 300°C. Armstrong and Bruce eventually managed to synthesise layered $LiMnO_2$ using the "soft chemistry" technique of a *chimie-douce* ion exchange reaction starting with α-$NaMnO_2$, the layered sodium analogue.

Initial electrochemical studies on this compound revealed the desired high voltage but poor cyclability caused by a tendency for the layered phase to revert to the spinel $LiMn_2O_4$. This has been alleviated through the substitution of chromium into the material[xiv] but the use of chromium is prohibited by environmental and economic considerations.

1.3.6 Iron Systems

Lithium ferrite ($LiFeO_2$) would be an attractive material as a cathode in a rechargeable battery from the point of view of its low cost and non-toxicity compared to $LiCoO_2$.

The synthesis of layered forms of $LiFeO_2$ has been achieved by various means including ion exchange from α-$NaFeO_2$ in molten salts[xv], from Fe(OOH) in non-aqueous solvents[xvi] and via hydrothermal methods with FeOOH and LiOH.

These techniques produce either corrugated layer $LiFeO_2$ or goethite type, which has a similar structure to the spinel phase of MnO_2. These phases have both been shown to be rechargeable in lithium cells but the amount of lithium that can be reversibly intercalated is small and cyclability is poor[xvi], and as a consequence the material is not in use in commercially available batteries.

Iron sulphates have also been investigated as hosts for lithium intercalation. The use of sulphates is an interesting tactic as this lowers the covalency of the Fe-O bond leading to a decrease in the energy of the Fermi level of the material and hence increasing the voltage of the couple.

Work by Stuart Licht in Israel has used the principle of using the high oxidation state of a transition metal ion to produce a high capacity battery, in their case the use of iron in its +6 oxidation state[xvii]. It was long believed that the Fe(VI) oxidation state offered no utility as a

battery material, based mainly on its instability in aqueous solutions. Licht found that $BaFeO_4$ and K_2FeO_4 are not only stable in an alkaline environment but actually increase in stability the more concentrated the alkali. Upon discharging these materials in an alkaline cell with a zinc anode $BaFeO_4$ gave an open cell voltage of 1.85V with a maximum energy capacity of 419Whr/kg. This appears favourable when compared to the Zn/MnO_2 system which generates a voltage of 1.5V and has an energy capacity of 323Wh/kg. If, however, you consider the respective masses of the two systems then the iron system offers little advantage, in terms of specific energy density, over the manganese system. For manufacturers considering the system the fatal flaw was the instability of the ferrates in contact with aqueous solution, possibly due to the susceptibility of the structure of isolated FeO_4^{2-} tetrahedra to hydrolysis. In general the search for improved cathode materials focuses on structures with infinitely linked metal-oxygen tetrahedra.

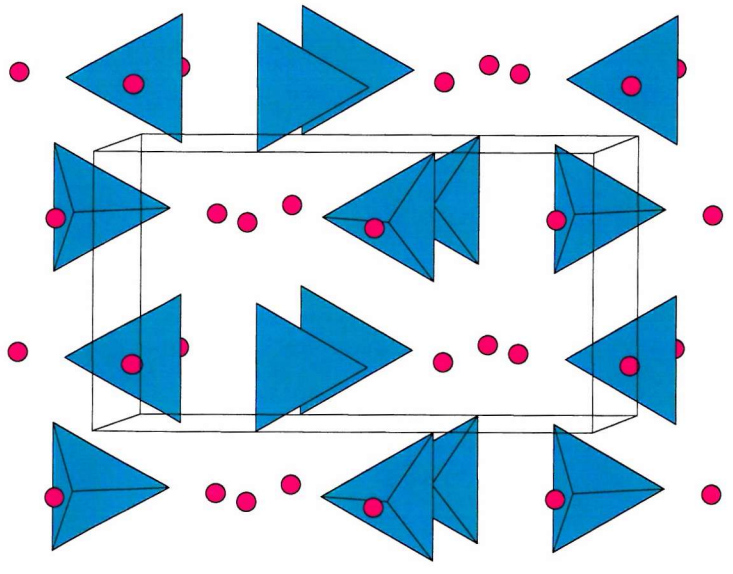

Figure 1-6: The structure of K_2FeO_4. FeO_4^{2-} tetrahedra (blue) Potassium ions (Purple)

We have already seen in §1.2.2 how the Fermi level of the cathode material is a factor in determining the voltage produced by the cell. Recently people have began applying the principle that in a system with M-O-X bonds the nature of X will, via an inductive effect, influence the balance between the ionic and covalent character of the metal-oxygen bond. This offers a method of systematically tuning the redox potential of the metal. This has lead to interest in materials such as iron phosphates and sulphates. The electron withdrawing effect of these groups reduces

the covalent character of the Fe-O interactions and causes a lowering of the energy of the antibonding d orbitals and therefore a higher cell voltage. In the case of iron(III) sulphate up to two lithium ions may be reversibly inserted reducing iron(III) to iron(II). The potential associated with this insertion is +3.6V vs. Li+/Li which is much higher than the couple in the simple iron oxide.

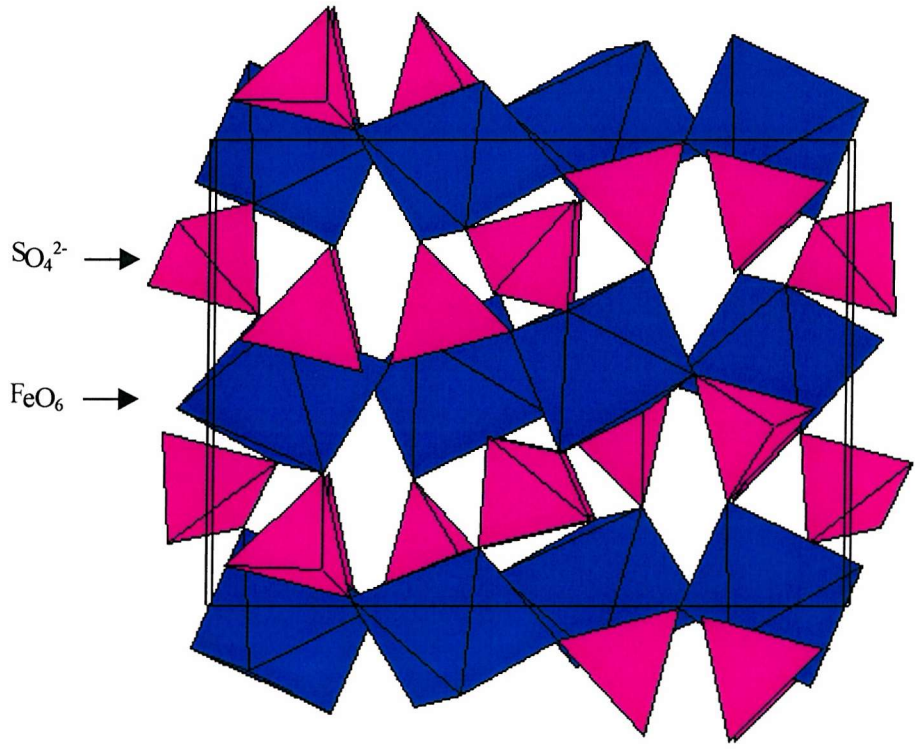

Figure 1-2: $Fe_2(SO_4)_3$. FeO_6 octahedra linked by corner-sharing through SO_4 tetrahedra.

1.4 CURRENT RESEARCH INTO HIGH OXIDATION STATE MATERIALS

1.4.1 $Li_2Mn_3O_7$

In the drive towards stabilising unusual transition metal oxidation states in novel materials it may be necessary to utilise unusual or new synthesis conditions. An example of this is the synthesis of $Na_2Mn_3O_7$, containing the Mn(IV) ion, by heating of the component oxides under high (1.4kBar) pressure and temperature[xviii]. A chimie-douce type replacement of the sodium ions with lithium has been undertaken to yield a new layered manganese compound that has a good capacity and retains this over at least 30 cycles. Innovative combinations of different techniques

such as in this example may be needed to make further progress in the synthesis of new insertion electrodes.

1.4.2 Bi(V) Compounds

Over the past ten years Kumada and Sleight have found simple low temperature hydrothermal methods to be very useful in synthesising the otherwise hard to obtain pentavalent form of bismuth. Compounds already produced include $LiBiO_3$[xix] and ABi_2O_6[xx] where A = Mg or Zn which adopts the trirutile structure, Figure 1-1. Assuming that the reduction of Bi(V) to Bi(0) is achievable in the cell then the uptake of electrons per atom per formula unit, 1.11 e per atom in ABi_2O_6, looks favourable compared to MnO_2 based systems. In addition Bismuth is generally accepted to be environmentally benign and is readily available. Its high atomic mass is an obvious drawback.

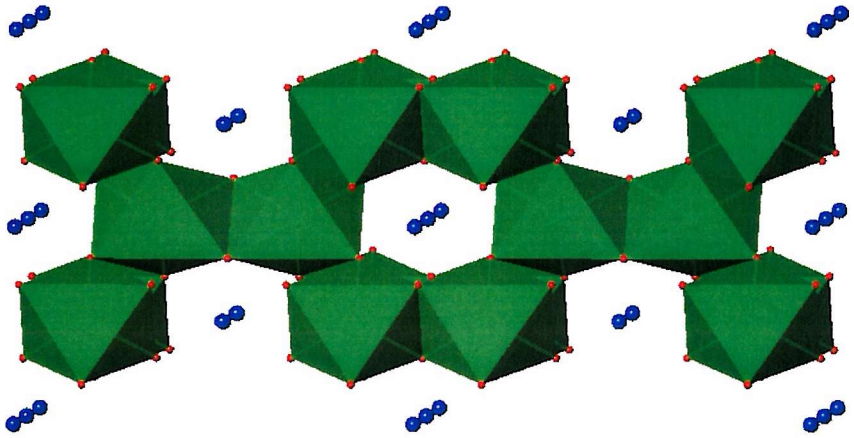

Figure 1-1: The tri-rutile structure of ABi_2O_6

Since the initial work on these compounds they appear to be little studied and no electrochemical studies have been performed. Sodium bismuthate, the starting material in the production of $MgBi_2O_6$ has been investigated with regards to its electrochemical[xxi] properties. These initial investigations observed two separate peaks in the cyclic voltammagram trace as the material was oxidised or reduced indicating that with bismuth (V) step wise discharge curves could be a problem.

1.5 THE SCOPE OF THIS WORK

From the discussion in §1.2.1 it is possible to identify a number of avenues which may lead to improved primary cell performance, for instance oxides have the low fermi level required of a cathode and first row transition metals are favourable because of their low weight and cost.

In general, the higher the oxidation state of the transition metal the greater the number of Li^+ charge carriers required to achieve charge neutrality and hence the greater the potential energy density. Battery manufacturers will refer to the electron uptake per atom in a formula unit, as this is related to energy density and provides a convenient method of comparison between materials. MnO_2 accepts one electron per Mn, or $0.33e^-$ per atom in the formula unit. It becomes a logical progression therefore to look for materials in which the metal ion may undergo a "greater" reduction, i.e. accept more electrons, which, assuming this can be achieved with minimal negative impact on potential and structural density, should improve energy density. Hence in the course of this project we will be targeting the synthesis of materials containing transition metals in high oxidation states such as Fe(IV), Mn(IV), Cu(III), and Bi(V). The strongly oxidising nature of such compounds has the added benefit of raising the half-cell potential of the cathode and therefore offers increased cell voltage[xxii].

This project will attempt to utilise unusual reaction conditions including hydrothermal synthesis and synthesis at high pressure and temperature to achieve these novel oxidation states. Work will focus in particular on bismuth, manganese and iron due to interesting advances made recently with these metals.

1.6 REFERENCES

[i] http://www.mindbranch.com/

[ii] Bruce P G, *Philos. Trans. R. Soc. Lond. A*, **354**, 1577, (1996)

[iii] ChabreY, Pannetier J, *Progress in Solid State Chemistry*, **23** (1): 1-130 (1995)

[iv] Dey A N, *Extended Abstr. Electrochem. Soc.* **54**, 132 (1973)

[v] Hunger H F, Heymach G J, *J. Electrochem. Soc.* **120**, 1161, (1973)

[vi] Ikeda H, *Lithium Batteries (edt. Gabano)* – Chapter 8 pg 181

[vii] Murphy D W, Di Salvo F J, Carides J N, Waszczak J V, *Mat. Res. Bull.*, **13**, 1395-1402, (1978)

[viii] Thackeray M M, *Prog. Solid St. Chem.*, **25**, 1-71, (1997)

[ix] Lavela, P., L. Sanchez, et al. *Jnl. Power Sources* **84** (1) 75-79 (1999)

[x] Nakamura H, Motooka K, et al *Jnl. Power Sources* **81-82** 632-636 (1999)

[xi] Thackeray M M, David W I F, Bruce P G, Goodenough J B, *Mat. Res. Bull.*, **18**, 461, (1983)

[xii] Manev V, Momchilov A, Nassalevska A, Sato A, *Jnl. Power Sources*, **54**, 323-328, (1995)

[xiii] Sun Y K, Jeon Y S, Lee H J, *Electrochemical and Solid State Letters*, **3**, 7-9 (2000)

[xiv] Pan C J, Lee Y J, Ammundsen B, Grey C P, *Chem. Mater.* **14**, 2289-2299 (2002)

[xv] Kanno R, Takayuki S, Yukishige I, Kawamoto Y, *Jnl Power Sources*, **68**, 145-152, (1997)

[xvi] Sakurai Y, Arai H, Okada S, Yamaki J, *Jnl Power Sources*, **68**, 711-715, (1997)

[xvii] Licht S, Wang B, Ghosh S, *Science*, **285**, 1039, (1999)

[xviii] Chang F, Jansen M, *Z. Anorg. Allg. Chem.* **531**, 177, (1985)

[xix] Kumada N, Takahashi N, Kinomura N, Sleight AW, *J. Solid State Chem.*, **126**, 121, (1996)

[xx] Kumada N, Takahashi N, Kinomura N, Sleight AW, *Mat. Res. Bull.* **32**, 8, 1003, (1997)

[xxi] Espinosa AM, San Jose MT, Tascon ML, Vasquez MD, Sanchez Batanero P, *Electrochim. Acta.*, **36**, 10, 1561, (1991)

[xxii] Koksbang R, Barker J, Shi H, Saidi M Y, *Solid state ionics,* **84**, 1-21, (1996)

2 Experimental Techniques

2.1 METHODS OF SYNTHESIS

2.1.1 Standard Ceramic Synthesis

The syntheses of the group 1 iron oxides (Chapter 4) were carried out using standard solid-state reactions. Generally speaking these reactions involve grinding together stoichiometric amounts of the component powders. The pressure and movement of the grinding serves multiple purposes, it reduces the powder particle size, it brings the particles of the constituent powders into intimate contact and in doing so reduces the size of any air cavities, and it encourages mixing of the powders so that the frequency of interfaces between the different reactants is maximised. Pelletisation of the powdered reaction mixture, typically at pressures of 10-15 tons further reduces the inter-particle separation and aids in the formation of homogenous, single-phase products. Each of these stages may be repeated at periods during a reaction if X-Ray diffraction indicates that it is necessary to achieve homogeneity, in particular regular regrinding of the mixture separates frontiers of the product phase that have formed and allows fresh reactants to come into contact. Reaction between the component powders occurs by ion diffusion between the reactant powders at their interfaces, hence the benefit of having many such junctions. Two major characteristics of these reactions may be explained as follows. The very high temperatures used are a result of the massive amount of energy required to disrupt the crystal lattice. Ionic attractions such as those in the lattice are the strongest of the four bonding types and this force is non-directional so one cation may be co-ordinated to as many as 12 anions. The characteristically long reaction times of ceramic synthesis reactions arise from the slow rate of ion-diffusion through the lattice structure, a process that is also speeded up by the high temperatures used.

2.1.2 Hydrothermal Synthesis

The reactions used to synthesise the bismuth compounds (Chapter 3) were carried out in hydrothermal bombs. This reaction method allows much lower reaction temperatures and times to be used as the reactants are solvated. In general particles in solution will have smaller particle size and an increased rate of diffusion, compared to that in their powdered state. High pressures are created by the vapour pressure of the solvent/air mixture in the limited space above the

solution, which again helps to compensate for the lower temperatures used and also speeds up the crystallisation process.

The general procedure for the hydrothermal bomb synthesis involved weighing out the starting materials and then transferring them directly to the Teflon bomb liner. In the case of a 75ml bomb, 30ml of solvent were added and the liner swirled by hand to aid dissolution of the powders. The liners were placed in the bombs and sealed. If water was being used as the solvent then the bombs were heated at temperatures of 110-150°C. If ethanol was used, as it was in the attempted solvothermal ion exchange, then the temperature was limited to 70°C and after the reaction period had expired the oven was turned off and the bomb left to cool in the oven.

2.1.2.1 High Pressure-High Temperature Hydrothermal Synthesis

In an attempt to synthesis novel manganese containing materials, (Chapter 5), a specially designed rig[i] was used which can achieve pressures of up to 3.6kBar at temperatures of 400 to 800°C, much higher than those that may be safely reached with the oven heated bombs used in the bismuth work.

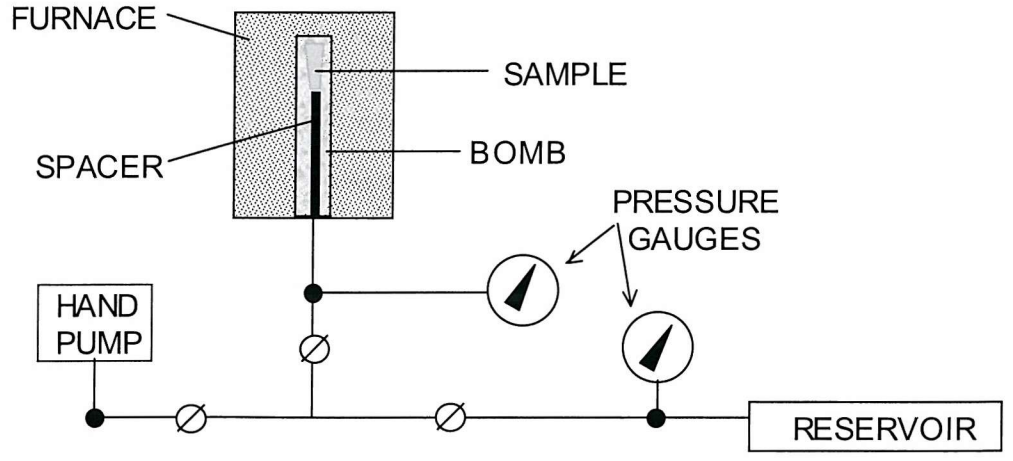

Figure 2-1: Schematic diagram of the high-pressure, high temperature hydrothermal apparatus.

In a typical experiment the reaction mixture was sealed into a 3cm long gold capsule by welding the capsule shut. The capsule was slid into the high-pressure bomb along with a spacer rod. The spacer rod serves the dual purpose of minimising the volume of high pressure water in the bomb and of keeping the sample located in a position close to the thermocouple probe so as to give an

accurate temperature reading for the reaction. The bomb is screwed onto its mounting on the rig, the furnace is lowered over the bomb and the safety door of the surrounding steel box is shut. The pressure in the system is increased to 7000psi by means of the hand pump and then all taps are shut and the system left to ensure no leaks are present. The furnace is then switched on and the system ramped stepwise to its reaction temperature and then left to equilibrate at this reaction temperature. Finally the hand pump is used to bring the system to the desired operating pressure. The pressure in the bomb could be continually monitored during the reaction via its individual pressure gauge. Any loss of pressure during the reaction indicated that the capsule had most likely burst, and the reaction could be halted.

2.1.3 Low temperature methods – ion exchange reactions

In most modern battery systems the lithium ion is the current carrier of choice as we have seen from the arguments in the introductory chapter. When it comes to designing new battery materials a common synthesis strategy is to form a product with a large cation such as potassium or magnesium at particular lattice sites or sometimes intercalated into the intra-lamellar spaces. It is then possible to form a potential battery material by inserting lithium into the structure or ideally replacing the large cation with lithium, and hopefully forming lithium-containing structures, which could not be synthesised directly. In the case of layered materials or materials where the cation is held in a cage like structure this ion-exchange may be achieved under relatively mild conditions with minimal disruption to the strongly bonded superstructure.

In the work presented here these ion-exchange reaction were attempted by refluxing the material undergoing the exchange with a lithium salt, generally a large excess of dry lithium bromide. These reactants were dissolved in anhydrous ethanol or hexanol along with a stoichiometric amount of cyclic-crown ether with a cavity size roughly matched to that of the ion being exchanged. The reflux was carried out under an atmosphere of dry nitrogen.

2.2 POWDER X-RAY DIFFRACTION

2.2.1 The theory

In a solid material the inter-atomic distances are of a similar order to the wavelength of radiation in the X-Ray region of the spectrum (ca. 10^{-10} m). This, as Max von Laue realised around 1920, means that X-rays should be diffracted upon passing through a material. It follows that a wave

diffracted by a crystalline material will have intensity and a direction which holds information on the ordered structure that diffracted it, however hard that information may be to extract.

The classic mathematical description of the X-ray diffraction experiment is as follows.

Consider a wave incident upon two atoms on adjacent lattice planes.

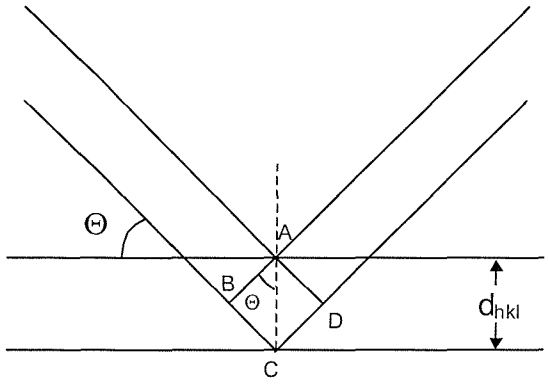

Figure 2-2: Diffraction from two point scatterers lying on parallel planes.

In order for the waves scattered from points A and C to be in phase the extra distance traveled by the wave diffracted from point C must equal a whole number of wavelengths. The factors that determine the size of this extra distance traveled are the incident angle of the wave, θ, and the separation, d_{hkl}, of the lattice planes, where h k and l are the miller indices of the of the planes. Simple trigonometry leads to the result;

$$BC + CD = n\lambda = 2.d_{hkl}.\sin\theta \qquad [2\text{-}1]$$

The Bragg Equation

where n is an integer and λ is the wavelength of the incident radiation.

In general the second order diffraction maximum from the 100 plane is equal to the first order maximum from the 200 plane and so on, therefore it is only necessary to consider the case where n=1.

An X-ray pattern, a plot of intensity vs. 2θ, can therefore reveal information about that structure which produced it, through a process known as indexing. Measurement of the X-ray maxima positions allows for calculation of the lattice plane separation d_{hkl}. The crystal system of the structure is then derived by identification of the lattice planes h, k, and l involved. Systematic

absences of certain diffraction maxima, caused by the presence of space symmetry elements in the particular lattice types, also aids in the identification of the crystal system.

Finally the lattice parameters for the structure are calculated using the correct expression for the particular crystal system. The lattice parameters are the points at which the plane *hkl* intersects the *a*, *b* and *c* axis.

Crystal system	*Expression for* d_{hkl}
Cubic	$\frac{1}{d^2_{hkl}} = \frac{h^2+k^2+l^2}{a^2}$
Tetragonal	$\frac{1}{d^2_{hkl}} = \frac{h^2+k^2}{a^2} + \frac{l^2}{c^2}$
Orthorhombic	$\frac{1}{d^2_{hkl}} = \frac{h^2}{a^2} + \frac{k^2}{b^2} + \frac{l^2}{c^2}$
Hexagonal	$\frac{1}{d^2_{hkl}} = \frac{4}{3}\left(\frac{h^2+hk+k^2}{a^2}\right) + \frac{l^2}{c^2}$
Monoclinic	$\frac{1}{d^2_{hkl}} = \frac{1}{\sin^2\beta}\left(\frac{h^2}{a^2} + \frac{k^2\sin^2\beta}{b^2} + \frac{l^2}{c^2} - \frac{2hl\cos\beta}{ac}\right)$
Triclinic	Complex expression

Table 2-1: Expressions relating d-spacings to lattice parameters, *a*, *b* and *c*, in the different crystal systems.

2.2.2 The experimental method

A powdered sample of a crystalline material contains a huge number of individual crystallites, orientated randomly with respect to the incoming X-ray radiation. Each of these individual crystallites will diffract the radiation according to the Bragg conditions. On average the crystallites in the sample will adopt every possible orientation, therefore the diffracted ray will emerge in all possible directions, for each of the allowed values of 2θ, and produce a cone of intensity at each diffraction maxima.

2.2.3 The instrumentation

An X-ray diffractometer consists of an X-ray source, a means of monochromating and focusing this source onto the sample stage, and a method of detecting the diffracted radiation.

In modern X-ray diffractometers the collection of experimental data is completely computer controlled. It involves the sample stage rotating at a rate, x, through an angle θ with respect to the fixed incoming radiation. Simultaneously the X-ray detector rotates about a circle with the sample stage at its centre, at a rate, $2x$, covering an angle 2θ. As the sample stage and detector precess stepwise over the user-defined angle range, the detector cuts through the cones of diffracted X-ray intensity. The 2θ values and the corresponding X-ray intensity at each angle are recorded onto a PC. The PC produced a plot of 2θ vs. intensity which constitutes the characteristic X-ray pattern of the sample under test.

Siemens D5000 and D8-Advance diffractometers were used in the course of this work. Phase identification scans were recorded over the 2θ range 20-60°, with a step-size of 0.02°. In the case of the Group 1 iron oxides work (Chapter 4) it was necessary to use a specialised detector, capable of screening out the fluorescence of the iron species. Furthermore when it came to recording data over the range 2θ=10-90° it was necessary to use a smaller stepsize of 0.01° to try and resolve the closely spaced peaks caused in the pattern of the orthorhombic systems which were distorted and close to fitting a cubic model.

2.2.4 The analysis

The recorded X-ray pattern can be electronically compared to patterns on JCPDS, a database containing patterns of known materials. If the comparison yields a similar structure then this likeness may be used as a starting model for refinement of the unknown's structure.

If no similar structure is found then lattice parameters must be found by indexing the pattern and recourse to the equations in §2.2.1. It is possible to perform this process electronically which uses statistical methods to refine the starting lattice parameters. This is useful as the most common cause of a Rietveld refinement diverging in the early stages of the process is a poor set of starting lattice parameters for the calculation. The CELLREF program uses an iterative least squares process to minimise the equation:-

$$M = \sum_i W_i (\sin^2_i \theta^{obs} - \sin^2_i \theta^{calc})^2 \qquad [2\text{-}2]$$

W_i = *a weighting factor*

M = *weighted minimised difference for observed 2Θ data*

2.3 POWDER NEUTRON DIFFRACTION

In the course of this work it has been necessary to collect powder neutron diffraction (PND) data on some of the samples synthesised, to complement and extend the information garnered from the laboratory X-ray studies.

The fundamental difference between the methods of powder X-ray diffraction (PXD) and PND is the method of scattering of the respective radiation, X-rays are scattered by the electron cloud surrounding the nuclei, neutrons are scattered by the nuclei themselves.

This fact has a number of important consequences;

- PND will tend to locate the positions of atoms, particularly those of low atomic number, with greater precision than PXD, nuclear density is smeared over a smaller area than is electron density.
- Thermal parameters obtained with PND will be smaller than those obtained by PXD, the motion of heavy nuclei is much less than that of light electrons, particularly if cryogenic methods are employed.
- There is no simple dependence between atomic number and scattering power in neutron diffraction because the total scattering by nuclei consists of a potential and a resonant contribution. Therefore a light atom such as hydrogen may scatter neutrons well and be observed whereas a heavy atom such as vanadium may have negligible scattering power with respect to neutrons and hence be used as a container for samples subjected to PND. This makes the technique useful for locating small, light atoms in the presence of larger, heavier ones.
- Scattering by the nuclei means it is possible to distinguish between atoms with very similar X-ray scattering powers such as Mn, Fe and Co and even between different isotopes of the same atom.
- Neutrons have an intrinsic magnetic moment and can simultaneously be used as a probe of a samples crystal and magnetic structure. This is relevant to the work on iron in Chapter 4.

The main drawbacks of neutron diffraction are the need for highly specialized, and therefore highly costly equipment and the low flux of neutron sources which requires long experiment times. Despite these the technique is invaluable as a probe of fine structural details and magnetic and isotopic effects.

2.3.1 *POLARIS – Time of Flight (TOF) PND*

The POLARIS instrument at the Rutherford Appleton Laboratory in Oxfordshire is a medium resolution instrument operating on the time of flight principle in order to distinguish between neutrons of different energies. Neutrons are produced in pulses by bombarding a heavy metal target with high energy particles. The neutrons so produced will have a range of wavelengths and according to the expression $c = \upsilon\lambda$, a corresponding range of speeds. They will therefore reach a fixed target at different times and this provides a means of selecting a specific neutron energy. We have already seen how in laboratory X-ray studies a monochromatic source of radiation is directed at a sample stage which is rotated through an angle 2θ and d is subsequently determined. In TOF neutron studies it is λ that is varied whilst the angle θ is fixed, Figure 2-3.

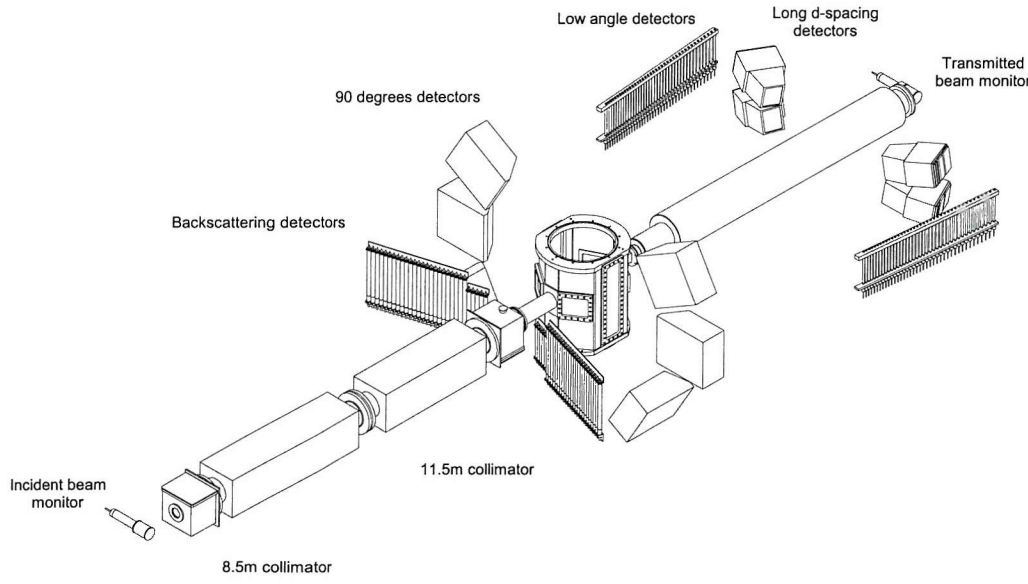

Figure 2-3: Schematic of POLARIS

POLARIS measures the Bragg reflections via detectors positioned at fixed scattering angles and monitors the time between the release of the burst of spallated neutrons and their arrival at the detectors. The relationship between TOF and d-spacing is linear and is derived by relating de Broglie's relationship and Bragg's Law;

$$\lambda = \frac{h}{m_n \upsilon_n} = 2d \sin\theta \qquad \textbf{[2-3]}$$

where h is Planck's constant, m_n and v_n are the mass and velocity of the neutron respectively (their product being the particle's momentum) and d and $sin\theta$ are as derived by Bragg's law.

Given that the primary flight path (moderator to sample) is labelled L_1, and the secondary flight path (sample to detector) is L_2 with corresponding flight times t_1 and t_2, then;

$$\frac{h}{m_n}\left[\frac{t_1+t_2}{L_1+L_2}\right] = 2d\sin\theta \qquad [2\text{-}4]$$

Therefore with a total neutron flight path L and time of flight t;

$$t = 2dL\left(\frac{m_n}{h}\right)\sin\theta \qquad [2\text{-}5]$$

$$\therefore \quad 1 \propto d$$

To give a rough idea of the timescales and resolutions involved, for POLARIS with a moderator to sample distance of 12m, a 1Å d-spacing reflection will be detected in a backscattering bank at a TOF of ~5000μs.

POLARIS data was collected from the backscattering C bank of detectors to yield the highest resolution data, useful in resolving peaks that were overlapping in "equivalent" X-ray patterns. Data from the low angle A bank, with poorer resolution but higher d-spacing reflections aided in the identification of accurate cell dimensions, space groups and magnetic reflections.

2.4 STRUCTURAL REFINEMENT – THE RIETVELD METHOD

The synthetic methods used in solid state chemistry, with their characteristically high temperatures and frequent regrinding of reactants, do generally yield single crystals with dimensions large enough ($0.01\,mm^3$) for analysis by single crystal X-ray diffraction methods.

H.M.Rietveld devised a method[ii] of structure determination which involves the refinement of a calculated profile so as to minimise the difference between the calculated and experimentally observed values. A starting point for the calculated profile is obtained, by comparison with a similar structure, and the relevant instrument parameters and lattice parameters obtained from CELREF indexing are entered. If the calculated profile has peak markers positioned in broad agreement with the peaks in the observed pattern, then the refinement process begins. The parameters that determine the peak shape of the calculated profile and the materials structure are, first individually and then in combination, tweaked until the least squares difference between the whole of the observed and the whole of the calculated pattern is minimised. When the goodness of fit cannot be improved any further, at which point the iterative calculation has hopefully converged, then the refinement is stopped and structural information may be extracted from the refined model.

This technique is applicable to X-ray, single-wavelength neutron and TOF neutron diffraction data.

2.4.1 The theory

It may be shown that for any regular array of stationary atoms, the structure factor F, is the sum of the contributions of the scattering amplitudes, b, and the phases, ϕ, of each atom[iii], leading to the expression.

$$F = \sum_{j=1}^{N} b_j \exp[i\phi_j] \qquad [2\text{-}6]$$

In a unit cell, the total phase shift of an atom j, at a point (x_j,y,z_j) from the origin is the sum of the phase shifts in each direction when the phase shift is evaluated, the structure factor for the unit cell becomes

$$F_{hkl} = \sum_{j=1}^{N} f_j \exp[2\pi i(hx_j + ky_j + lz_j] \qquad [2\text{-}7]$$

where h, k, and l are the Miller indices that define the plane from which the reflection takes place. For very small crystals, it may be shown that the intensity of the scattered beam is proportional to the square of the structure factor.

$$I_{hkl} = kL^2|F_{hkl}|^2 \qquad [2\text{-}8]$$

where k is a scaling constant and L is the Lorentz factor, a geometric function of the method of data collection and hence the instrument used. In real crystals the scattered intensity is modified by imperfections in the lattice structure. Defects and substitutional disorder cause local structural irregularities, particularly in non-stoichiometric materials. In addition, thermal motion causes a reduction in scattered intensity as a result of time independent vibrations of the atoms about their mean positions. Consequently the atoms in a plane are displaced randomly from their ideal in plane positions, disrupting the in-phase behaviour of their combined scattering. The correction to a structure factor reflected by a plane hkl is of the form[iv]

$$T_{hkl} = \exp\left[-B_{hkl}\frac{\sin^2\theta}{\lambda^2}\right] \qquad [2\text{-}9]$$

so that for a unit cell the structure becomes

$$F_{hkl} = \sum_{j=1}^{N} b_j n_j \exp\left[-B_j \frac{\sin^2\theta}{\lambda^2}\right] \exp\left[2\pi i(hx_j + ky_j + lz_j\right] \quad \text{[2-10]}$$

where n_j is the occupation factor of the jth atom, equal to one in the structure free defects. This expression assumes isotropic broadening which was the model used for the thermal parameters throughout this work.

2.4.2 *The general process*

1) Select an approximate starting model of the unknown structure by comparison with the patterns of known structures.
2) Refine the scale factor and background parameters
3) Refine the lattice parameters, zero point error and possible sample displacement correction in order to accurately locate the Bragg reflections. Preliminary refinement of peak shape parameters.
4) Locate atoms by allowing their positions to vary. This stage alters peak intensities and should improve the peak shape.
5) Once the atom positions are stable refine the isotropic temperature factors.
6) Complete the refinement of the peak shape parameters and also add in any necessary factors such as asymmetry or preferred orientation parameters.
7) In the case of neutron data it may be possible to refine the anisotropic temperature factors.

2.4.3 *X-Ray Data Refinement*

The quantity minimised over the course of a Rietveld least squares refinement is the function M, the sum over all data points

$$M = \sum_{i=1}^{N} \omega_i \left(y_i^{obs} - y_i^{calc}\right)^2 \quad \text{[2-11]}$$

where ω_i is a weighting factor denoted by $1/y_i$ and y_i^{obs} and y_i^{calc} are the observed and calculated intensity at each step point i ($2\theta_i$ for PXD). The calculated intensities y_i^{calc} are determined from the structural model by summing the calculated contributions from neighbouring Bragg reflections (k) plus the background b_i

$$y_i^{calc} = s\sum_k L_k |F|^2 \phi(2\theta_i - 2\theta_k) P_k A + y_{bi} \quad [2\text{-}12]$$

where s = scale factor

L_k contains the Lorentz polarisation and multiplicity factors

ϕ = reflection profile function

F_k = structure factor for the *k*th Bragg reflection

P_k = preferred orientation function

A = absorption factor

Y_{bi} = background intensity at the *i*th step

The background intensity at $2\theta_i$ is obtained from a specified, refineable background function.

$$y_{bi} = \sum_{m=0}^{5} B_m \left[\frac{2\theta_i}{BKPOS} - 1\right]^m \quad [2\text{-}13]$$

where *BKPOS* is the background position that is user-specified in the background control file. Since a comparison of intensities is performed at every point, it is essential for the construction of the calculated profile to accurately describe the shape of the Bragg reflections *i.e.* peak shape. Peak shape is generally dictated by the instrument; in the case of the Siemens instruments used the peak shape is pseudo-Voigt, and is described by the function

$$\eta L + (1-\eta)G \quad [2\text{-}14]$$

where L and G are the Lorentzian and Gaussian contributions to the peak shape and η is the mixing parameter which can be refined as a linear function of 2θ;

$$\eta = N_A + N_B(2\theta) \quad [2\text{-}15]$$

where N_A and N_B are refinable parameters.

The Gaussian (G) and Lorentzian (L) contributions to the peak shape are represented by the equations;

$$G = \frac{(4\ln 2)^{\frac{1}{2}}}{H_k\sqrt{\pi}} \exp\left(-4\ln 2(2\theta_i - 2\theta_k)^2 / H_k^2\right) \quad [2\text{-}16]$$

and

$$L = \frac{2}{\pi H_k} \Big/ \left[1 + 4\frac{(2\theta_i - 2\theta_k)^2}{H_k^2}\right] \quad [2\text{-}17]$$

where $2\theta_k$ is the calculated position for the *k*th Bragg peak corrected for the counter zeropoint and H_k is the full-width-at-half-maximum (FWHM) of the *k*th Bragg reflection.

The FWHM, H_k, of a peak varies with the scattering angle $2\theta_k$ and is modelled as

$$H_k^2 = U\tan^2\theta + V\tan\theta + W \qquad [2\text{-}18]$$

where U, V and W are the refineable parameters dependent upon both the instrument and sample. This formula therefore explains the peak broadening effect of a samples particle size and also the observation that at low scattering angles the peak shape shows significant asymmetry due to the detector and sample heights.

The refineable parameters for any least squares refinement fall into two distinct groups. The first group defines the structural parameters which describe the contents of the unit cell and include the overall temperature factors, co-ordinates and occupancies of each atom. The second group contains the profile parameters which define the position, shape and FWHM of each peak and consist of the profile scale factor, unit cell parameters, U, V, W, zeropoint, asymmetry and preferred orientation correction. In order to make a quantitative assessment of the agreement between the observed and calculated profiles, a number of reliability factors are defined, $R_{profile}$, $R_{expected}$, $R_{weighted\ profile}$.

So far we have assumed that the thermal displacements are isotropic but this is rarely the case except for highly symmetrical special sites of cubic space groups.

The R-factors are given by;

$$R_{profile} = R_p = 100\left[\frac{\sum_i \left|y_i^{obs} - y_i^{calc}\right|}{\sum_i y_i^{obs}}\right] \qquad [2\text{-}19]$$

$$R_{expected} = R_{exp} = 100\left[\frac{(N-P+C)}{\sum_i \omega_i (y_i^{obs})^2}\right]^{1/2} \qquad [2\text{-}20]$$

Where R_{exp} is obtained from the statistics of the refinement and N is the number of observations, P is the number of refineable parameters and C is the number of constraints.

The most meaningful of the 3 R-factors, in both mathematical terms and in terms of reflecting the progress of a refinement, is the $R_{weighted\ profile}$ (R_{wp}) because the numerator is the residual being minimised.

$$R_{wp} = 100\left[\frac{\sum_i \omega_i \left[y_i^{obs} - y_i^{calc}\right]^2}{\sum_i \omega_i \left[y_i^{obs}\right]^2}\right] \quad [2\text{-}21]$$

The final measure of the whole fit that is minimised during the refinement is the chi-squared parameter, defined as;

$$\chi^2 = \left[\frac{R_{weightedprofile}}{R_{\exp}}\right]^2 \quad [2\text{-}22]$$

Therefore for a good fit, the $R_{weighted\ profile}$ should approach the statistically expected R-factor (R_{exp}). The goodness of fit can also be measured by examining a plot of profile fit; for a good fit, the difference line between the calculated and observed patterns should be as flat as possible. All Rietveld refinements presented in this thesis were performed using the GSAS suite of programs[v].

2.4.4 Neutron Data Refinement

The refinement of neutron diffraction data is in some respects made easier by some of the innate features of the diffraction of neutrons compared to X-rays. There is no form factor associated with the scattering of neutrons and consequently a data set may be collected over a much larger angular range. Preferred orientation effects are reduced due to the nature of the sample mounting in a neutron diffraction experiment, and although it varies from instrument to instrument the resolving power of neutron techniques are far greater than those of laboratory X-ray analysis. This combination of features permits the determination of atomic coordinates and temperature factors with high precision, resulting in good refinement statistics, and high accuracy.

The TOF PND data collected on POLARIS was refined using GSAS using the Rietveld technique as previously discussed. The TOF data plotted along the x-axis is converted to d-spacing using [2-23].

$$t = \frac{2dm_n l \sin\theta}{h} \quad [2\text{-}23]$$

where m_n is the mass of the neutron, l is the total neutron flight path, 2θ the scattering angle and h is Planck's constant.

A d-spacing dependent absorption correction has to be applied to data used in these refinements due to the range of incident neutron energies employed. In addition, the peak shape is more

complex and is often fitted in terms of Gaussian, Lorentzian and exponential expressions. Background is fitted using a simple polynomial expression typically described by five terms.

2.5 ENERGY DISPERSIVE X-RAY SPECTROSCOPY

Scanning electron microscopy (SEM) uses an electron beam to illuminate solids rather than visible light, to build an image of the surface topography. This particular technique was not used in the work presented in this report but an extension of it, energy dispersive X-ray spectroscopy (EDAX) was used. When energetic electrons such as those created in the beam of an SEM instrument are incident upon a sample several processes occur. EDAX detects one of these processes, the X-rays released when an outer shell electron "falls" into the hole created by the expulsion of a inner shell electrons under the force of the electron bombardment. The energy of the X-rays so released is characteristic of the element from which it emanated. A plot of x-ray energy against intensity can therefore provide qualitative and quantitative information on the composition of the sample. Despite the large errors associated with this technique it provides a cheap and quick insight into the composition of a material and can indicate whether further investigation is worthwhile. The technique proved useful in indicating whether lithium ion exchange reactions had been successful, where a full neutron analysis for example could not be justified.

2.6 REFERENCES

[i] Weller M T, Dann S E, Henry P F, Currie D B, *J. Mat. Chem.* **9**, (1999), 283.

[ii] Rietveld H M, *Acta. Cryst.* **22**, (1967) 151

[iii] Buerger M J, *Contemporary Crystallography*, McGraw-Hill (1970)

[iv] Young R A (Ed), *The Rietveld Method*, Oxford University Press (1995)

[v] Larson A C, Von Dreele R B, Generalised Structure Analysis System, MS-H805 Los Alamos, NM87545, (1990)

3 Hydrothermal Preparation of Bismuth (V) Compounds

3.1 INTRODUCTION

Bismuth is a metal which may, if prepared in a suitably stable high oxidation state, offer a potentially large sink for electrons if it could be reduced from Bi(V) to Bi(III) or ideally to Bi(0). Bismuth is environmentally benign enough to be used in medical applications and as a replacement for lead shot although a drawback in terms of battery materials is its large mass.

Bismuth is commonly found in its +3 oxidation state with the +5 form being much more of a rarity, infact as recently as 1991 the only well determined structure of a Bi(V) compound was Na_3BiO_4[i]. Since then a number of methods for obtaining compounds containing the stable Bi(V) ion have been developed.

In 1991 Carlson and Stacy synthesised six new bismuth (V) compounds by precipitation from molten solution[ii], Table 3-1. The compounds precipitated out as transparent yellow crystals and solution of the structures via single crystal X-Ray diffraction techniques found that the compounds crystallised in one of three new structure types. The compounds were all hygroscopic but otherwise reported to be stable under ambient conditions. This work provided the first evidence that the bismuth (V) ion could be formed and stabilised in a variety of structures. It also showed that Bi(V) will preferentially coordinate to six oxygen atoms and in some cases these polyhedra would share corners, indicating the possibility that chains of BiO_6, of the type desirable in battery materials, could form.

Material	Melt Constituents			Structure
$NaBa_3BiO_6$	NaOH	$Ba(OH)_2$	Bi_2O_3	Rhombohedral unit cell. $NaBiO_6^{6-}$ chains with Ba atoms located between chains.
$NaSr_3BiO_6$	NaOH	$Sr(OH)_2$	Bi_2O_3	$NaBa_3BiO_6$ type
$LiSr_3BiO_6$	LiOH	$Sr(OH)_2$	Bi_2O_3	Triclinic unit cell (distorted $NaBa_3BiO_6$)
Li_6KBiO_6	LiOH	KOH	Bi_2O_3	Rhombohedral unit cell. Icosohedra of 12 O atoms surrounding K in centre of cell. Li cap the faces of the icosohedra and Bi is sited at the cell origin.
Li_6RbBiO_6	LiOH	RbOH	Bi_2O_3	Li_6KBiO_6 type
$LiBa_5Bi_2O_{11}$	LiOH	$Ba(OH)_2$	Bi_2O_3	Orthorhombic unit cell. 8 barium atoms define a cube through which run chains of corner sharing BiO_6 octahedra. Li and excess O are located between the chains.

Table 3-1 : The Bismuth (V) oxides prepared by Carlson and Stacy in 1991.

A second favourable indicator of the possible utility of the Bi(V) ion in battery materials is the ion conductivity exhibited by $KBiO_3$[iii], Figure 3-1. This material was prepared using the technique of electrocrystallisation from a flux of Bi_2O_3, $ZnCl_2$ and KOH at 175°C. Again corner, and this time also edge, sharing BiO_6^{7-} octahedra can be seen in the structure. Conductivity measurements indicate that the potassium ions are mobile but the low conductivity (10^{-5} S/cm @ 300°C) is presumably due to the potassium ion's role in stabilising the structure.

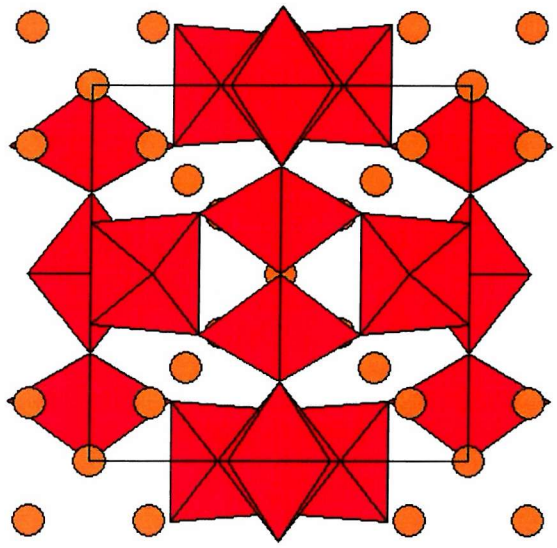

Figure 3-1 : The tunnel structure of $KBiO_3$

The lithium analogue of $KBiO_3$ has been produced by hydrothermal synthesis, a technique that has proved to be particularly successful in the investigation of Bi(V) compounds. In a relatively short time Kumada *et al.* have used variations on a theme of the reaction of $NaBiO_3.6H_2O$ with group 1 and 2 salts in water to synthesise a variety of new materials, including Ca, Sr, and Ba pyrochlore type structures containing Bi(V)[iv], mixed +3/+5 valent Bi_2O_4[v], $LiBiO_3$[vi], and ABi_2O_6 (A=Mg,Zn)[vii]. The initial serendipitous investigations, which produced a variety of products in the reaction bomb, have been honed so that the reaction conditions may be chosen so as to target the formation of particular phases from the solution.

The utility of the hydrothermal method of synthesis lies in the fact that the low temperatures used in the synthesis are less destabilising to the +5 oxidation state of bismuth than traditional solid state methods and the likelihood of reduction of bismuth to the +3 state in these cases is reduced. Hydrothermal methods have the added benefit in terms of our research in that they generally

result in products with small particle sizes, due to the dissolution of the reactants. Small particle size is considered to be a desirable feature in battery materials.

The preparations of the alkaline earth containing, pyrochlore type materials, were achieved by heating combinations the respective alkaline earth nitrate with hydrated $NaBiO_3$ in a hydrothermal bomb at temperatures of 120-180°C for 2 days to give $A_xBi_yO_{7-3\delta}(CO_3)_\delta$ for A= Ca, Sr and $Ba_{0.68}Bi_{3.05}O_{6.41}(H_2O, OH)_{0.59}$. These stoichiometries were inferred from DTA data and only the strontium structure was confirmed through Rietveld refinement as the authors report that the space group of the distorted pyrochlore structure, which they presumed formed in the case of calcium and barium, was unknown.

The structures of $LiBiO_3$ and ABi_2O_6 (A=Mg,Zn), with their system of channels containing the counter-cation, look to be suitable for incorporation of more lithium ions, as required when charging a battery material although no electrochemical studies have been carried out on these materials.

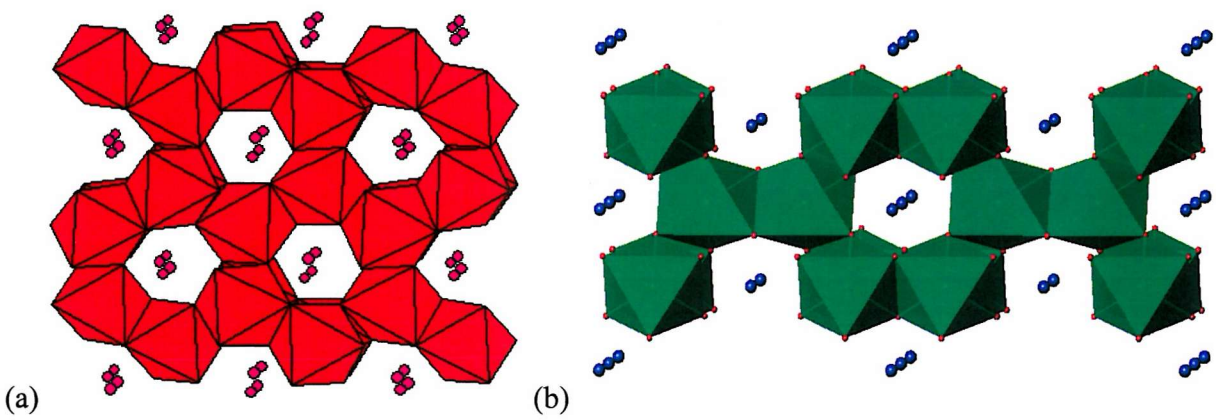

Figure 3-2: The structures of (a) orthorhombic $LiBiO_3$ (b) Tetragonal $MgBi_2O_6$

Bi(V) Material	Hydrothermal Reaction Conditions	Ratio	Crystal
$Ca_xBi_yO_{7-3\delta}(CO_3)_\delta$	$Ca(NO_3)_2.nH_2O + NaBiO_3.nH_2O$ 180°C, 2days	Ca/Bi = 4	Monoclinic a=10.83Å
$Sr_xBi_yO_{7-3\delta}(CO_3)_\delta$	$Sr(NO_3)_2.nH_2O + NaBiO_3.nH_2O$ 180°C, 2days	Sr/Bi = 4	Cubic a=11Å
$Ba_{0.68}Bi_{3.05}O_{6.41}(H_2O,OH)_{0.59}$	$Ba(NO_3)_2.nH_2O + NaBiO_3.nH_2O$ 1st stage: 120°C, 2days 2nd stage: add $BaNO_3$, 180°C, 2days	Ba/Bi = 2	Tetragonal a=10.83Å, c=10.96Å
$LiBiO_3$	$LiOH + NaBiO_3.nH_2O$ 120°C, 2days	Li/Bi = 4	Orthorhombic a=8.8278Å, b=4.9135Å c=10.6914Å
$MgBi_2O_6$	$MgCl_2.6H_2O + NaBiO_3.nH_2O$ 130°C, 2 days	Mg/Bi = 4	Tetragonal a=4.8260Å, c=9.7190Å
$ZnBi_2O_6$	$ZnCl_2.6H_2O + NaBiO_3.nH_2O$ 90°C, 2 days	Zn/Bi = 1	Tetragonal a=4.8386Å, c=9.7422Å

Table 3-2: The range of bismuth (V) containing compounds synthesised by Kumada and Sleight *et al.*

3.2 EXPERIMENTAL

Our initial work in this area aimed to replicate the results of Kumada in terms of the hydrothermal synthesis of bismuth (V) containing compounds. It was hoped that work would continue with the replacement of the counter-cations by different species.

In all reactions the starting material of $NaBiO_3.nH_2O$ was supplied by Aldrich, X-ray analysis indicated that n=2. The general procedure for all reactions was to dissolve the starting materials in 30ml of water in the Teflon liner of the hydrothermal bomb. It was found that there was no benefit obtained from stirring the reaction mixture first so this was stopped to decrease the risk of contamination from the stirrer bar. The bomb was then screwed shut and placed into the oven. The products were filtered and washed with water and then dried at 110°C overnight. Kumada reported a centrifuging phase preceding filtering but this was attempted and there was no seperation of the solid products so this stage was omitted in all future syntheses.

3.2.1 $MgBi_2O_6$

The starting materials in the synthesis were sodium bismuthate (V) hydrate and the hexahydrate chloride salt of magnesium (Mg/Bi = 4). Optimal conditions for obtaining single phase $MgBi_2O_6$ were, for a 45ml bomb, a reaction temperature of 110°C for 7 days. Kumada found that a temperature of 130°C for 2 days gave the pure phase but when this was tried under identical conditions it was found that a large amount of impurity had formed. The impurity appeared as distinct orange crystals believed, from their X-ray pattern, to be Bi_2O_3.

3.2.2 $ZnBi_2O_6$

The synthesis of $ZnBi_2O_6$ as reported by Kumada could not be repeated by us under the same conditions or indeed under a wide variety of other reaction conditions attempted. X-ray patterns of the resulting powders indicated, that from the starting materials of $ZnCl_2$ and $NaBiO_3$, a mixture of zinc and bismuth oxides had formed.

3.2.3 $Ca_2Bi_2O_7$

Calcium chloride dihydrate and sodium bismuthate were mixed in the ratio Ca/Bi = 4. Optimal conditions for the formation of a single phase with an X-ray pattern indicative of a pyrochlore structure were found to be a reaction temperature of 150°C for 2 days.

3.2.4 $Sr_2Bi_2O_7$

Strontium chloride hexahydrate and sodium bismuthate were mixed in the ratio Sr/Bi = 4. Optimal conditions for the formation of a single phase with an X-ray pattern indicative of a pyrochlore structure were found to be a reaction temperature of 180°C for 2 days.

3.2.5 $Ba_2Bi_2O_7$

Kumada reports that synthesis of the barium pyrochlore structure required a second stage where more of the barium source, the nitrate of chloride salt, was added and then heated again. We could not replicate any conditions whereby the single phase barium pyrochlore structure was formed. X-ray patterns of the products from these attempts gave very broad, noisy peaks which bore no relation to those reported by Kumada.

3.2.6 Mn, Ni, Cd, La

Attempts were made to incorporate manganese, nickel and lanthanum into the bismuth(V) materials with no success. X-ray patterns of the products generally indicated the formation of Bi_2O_3. Indeed Kumada indicated his intention to try and substitute other cations into the materials in 1997 but has not reported any such work since then.

3.3 RESULTS

3.3.1 $MgBi_2O_6$

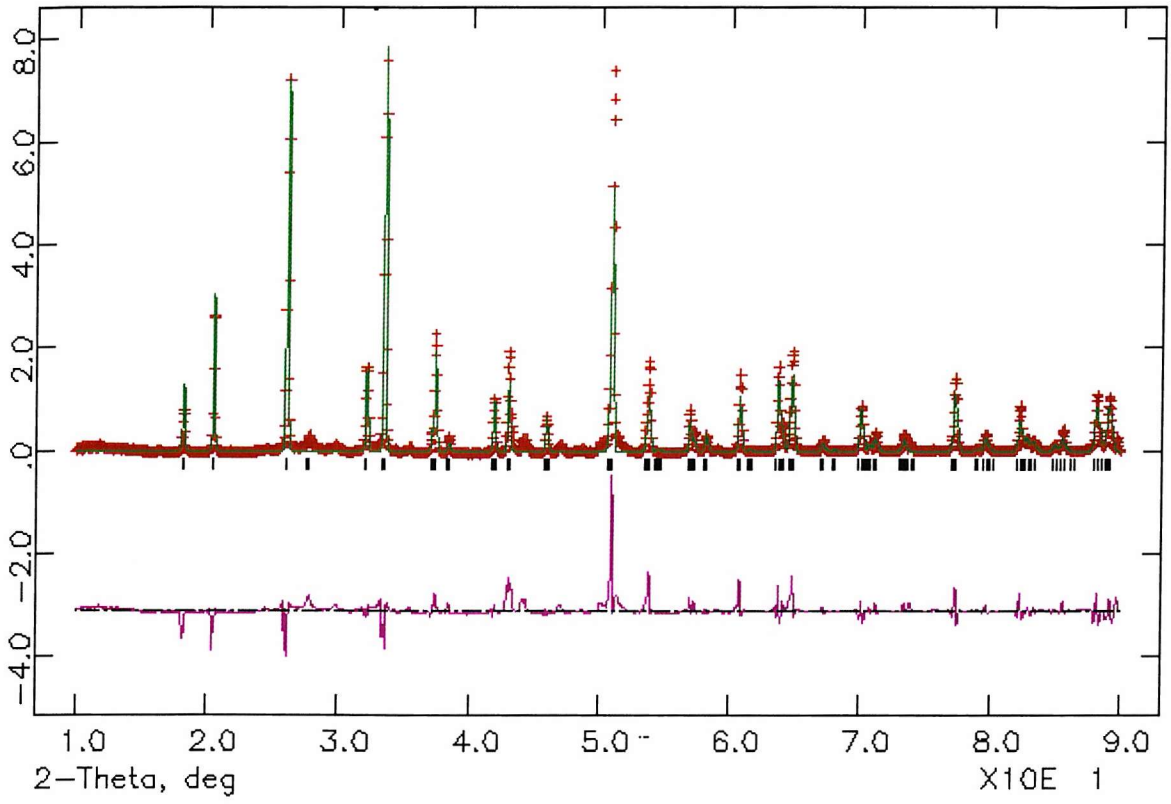

Figure 3-1: Observed (red crosses) and calculated (green line) X-ray diffraction pattern of $Mg_2Bi_2O_7$. The purple line is the value obs-calc. $R_{wp} = 16.93$, $\chi^2 = 159.3$ for 1860 observations and 23 variables.

The attempt at refining this structure, Figure 3-1, gives a fit only sufficient enough to indicate that the desired phase has been formed, no structural information may be obtained from the data. The model and lattice parameters used as starting point were obtained from the neutron data in reference vii. The zero point was refined and then fixed and profile coefficients were then varied systematically, with all those that tended to zero being fixed at that value.

3.3.2 $Ca_2Bi_2O_7$

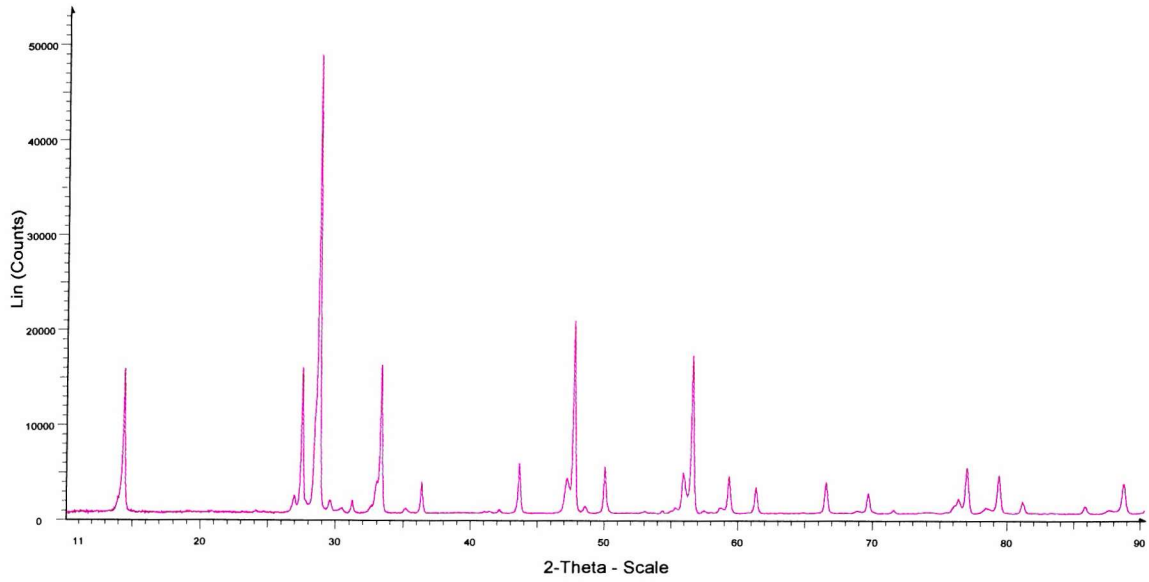

Figure 3-1:The X-ray pattern of $Ca_2Bi_2O_7$, indicative of a pyrochlore structure.

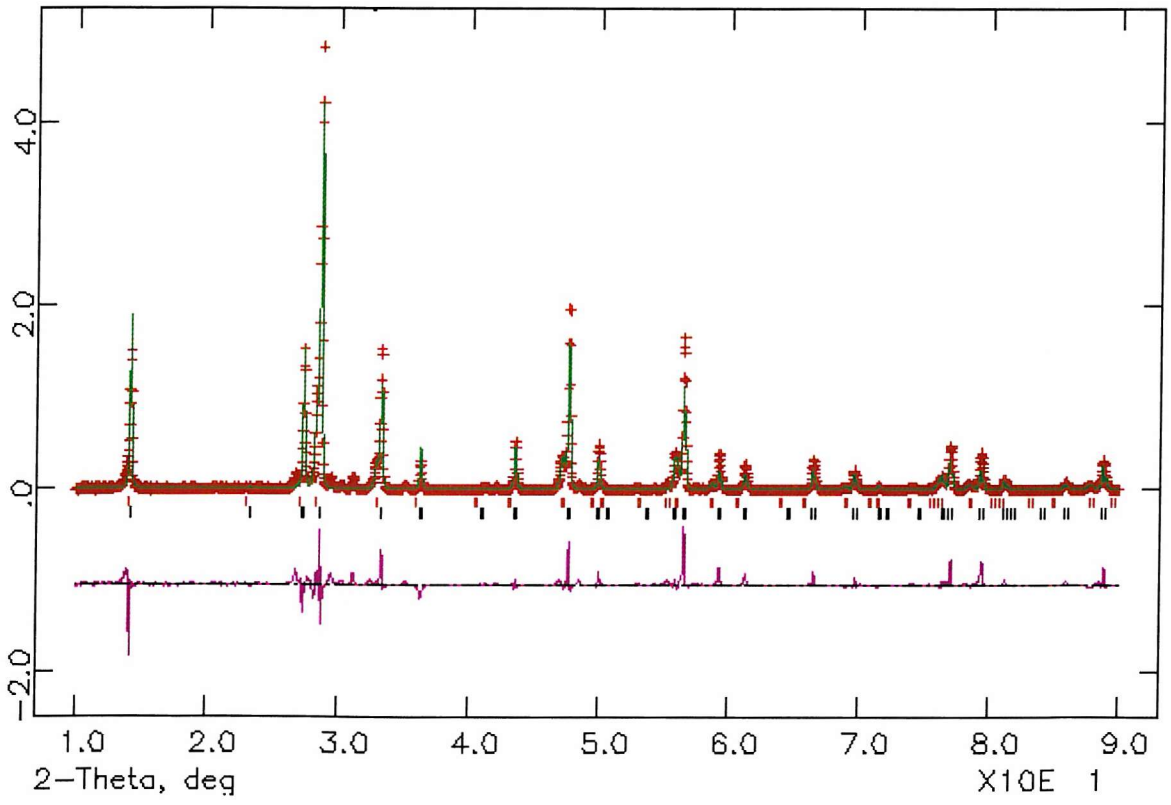

Figure 3-2: Observed (red crosses) and calculated (green line) X-ray diffraction pattern of $Ca_2Bi_2O_7$. Black tick marks are the reflections calculated to arise from the $Ca_2Bi_2O_7$ pyrochlore, red tick marks mark reflections from sodium doped bismuth oxide. The purple line is the value obs-calc. R_{wp} = 19.37, χ^2 = 51.66 for 4571 observations and 12 variables. Space Group Fd3m a=10.802(4).

Refinement of the calcium bismuth pyrochlore structure was not reported in reference iv, as the authors stated that the space group of the distorted pyrochlore structure was unknown. As a starting point for our refinement of the structure we used the atomic positions of the pyrochlore $Cd_2Re_2O_7$ and obtained lattice parameters by indexing the pattern in the same cubic space group used in the strontium case, $Fd\bar{3}m$. There was an appreciable amount of an impurity present which was modelled as a 0.2 phase fraction of sodium doped bismuth oxide. Lattice parameters obtained from the indexing of the pattern were first varied and their values remained reasonable so the zero point was varied and then fixed. Profile coefficients were varied. The thermal parameters of the bismuth and calcium were fixed at 0.02 and the calcium and bismuth positions were varied. Attempting to refine the fractional occupancy of the calcium site gave an occupancy greater than one which is physically meaningless. This result indicates that there may be a mixing of bismuth and calcium between the A and B sites or that the material is calcium defficient, which the calculation attempts to model by increasing the occupancy above one so increasing the scattering power of the site to that expected for full occupancy. The fit is not good enough to extract bond lengths and angles from but the overall tendency is towards a distortion of the pyrochlore structure of the cadmium rhenate.

3.3.3 $Sr_2Bi_2O_7$

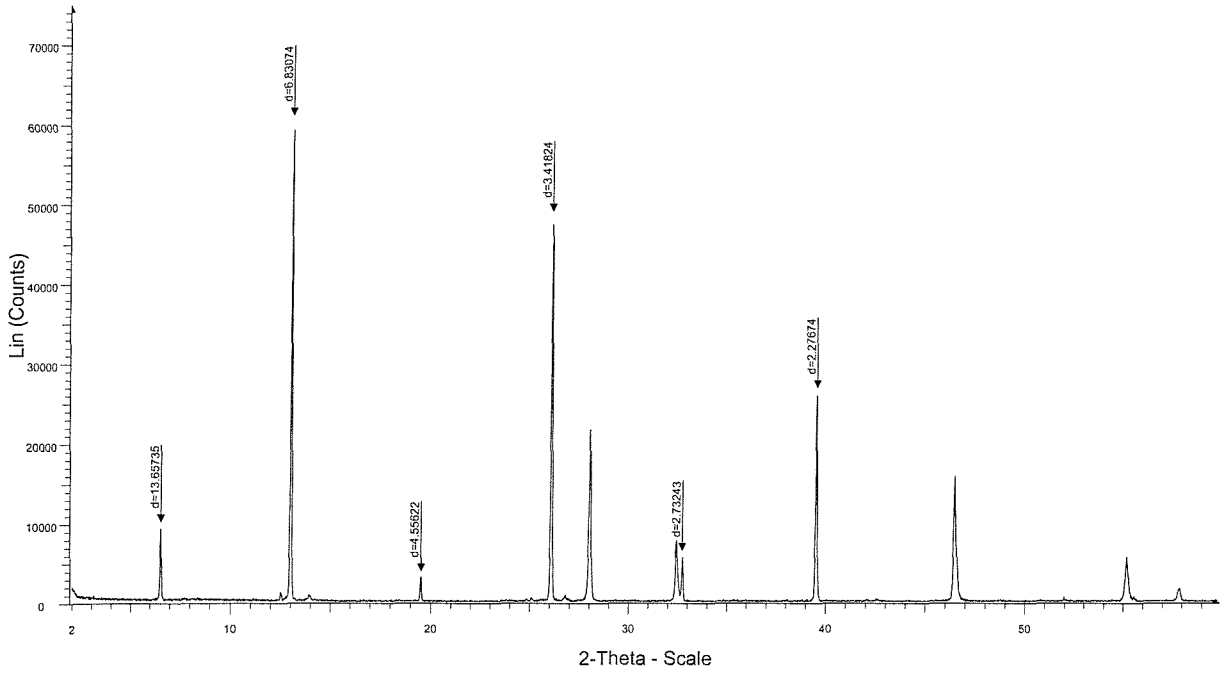

Figure 3-6:The low angle X-Ray pattern of $Sr_2Bi_2O_7$

The pattern obtained from the strontium containing sample was vastly different to that reported by Kumada et al. The ratio of the lowest angle peaks d-value to that of the other dominant peaks is an integer value, Table 3-3, and this indicates a layered structure. The pattern is similar to that of Lithium Niobium Uranium Oxide hydrate[1] which could be used as a starting model for any future studies of the structure.

d-spacing /Å	Ratio
13.65735	1
6.83074	2
4.55622	3
3.41824	4
2.73243	5
2.27674	6
1.94735	7

Table 3-3: The ratio of the d-spacings of the strontium containing product.

[1] JCPDS PDF No. 490153

3.4 CONCLUSIONS

Our work on the chemistry of bismuth (V) compounds has reproduced some of the compounds synthesised hydrothermally by Kumada et al. but never really with the same success at obtaining a clean single phase, as their results seem to indicate they did. The lack of single phase products was a major reason why electrochemical studies were not carried out on products resulting from these experiments.

The most interesting results arising from this work are those from the calcium and strontium containing materials. We were able to model the calcium bismuth oxide compound not modelled by Kumada and the results suggested a distorted pyrochlore structure. Our results indicated crystallisation in a cubic space group, rather than the monoclinic system suggested by Kumada.

The strontium compound appeared to form a layered material. Any new layered structures are always of interest in solid state chemistry and this synthesis should be repeated to confirm the results and investigate the structure of the material further.

3.5 REFERENCES

[i] Schwedes V B, Hoppe R, *Z. Anorg. Allg. Chem.* **393**, 136 (1972)

[ii] Carlson V, Stacy A M, *J. Sol. State Chem.* **96**, 332-343 (1992)

[iii] Nguyen T N, Giaquinta D M, Davis W M, Conrad zur Loye H, *Chem. Mater.* **5**, 1273-1276, (1993)

[iv] Kumada N, Hosada M, Kinomura N, *J. Sol. State Chem.*, **106**, 476-484, (1993)

[v] Kumada N, Kinomura N, Woodward P M, Sleight A W, *J. Sol. State Chem.*, **116**, 281-285, (1995)

[vi] Kumada N, Takahashi N, Kinomura N, Sleight AW, *J. Sol. State Chem.*, **126**, 121-126, (1996)

[vii] Kumada N, Takahashi N, Kinomura N, Sleight A W, *Mat. Res. Bull.* **32**, 8, 1003-1008, (1997)

4 The Preparation and Characterisation of $MFeO_2$ (M = K, Rb, Cs)

4.1 INTRODUCTION

At first sight the attractive features of $LiFeO_2$ as a cathode material are threefold, it has low cost, weight and toxicity. To this end there has been some interest in preparing a form of the compound with a structure like that of the manganese and cobalt equivalents, with layers of infinitely linked iron-oxygen octahedra.

The first strategies for achieving layered $LiFeO_2$ used ionic exchange reactions in molten salts starting from the sodium layered equivalent, α-$NaFeO_2$ [i], this form was found not to be electrochemically active however. Alternative strategies used the hydrothermal treatment of the iron (III) compounds FeOOH or $FeCl_3.6H_2O$ with a large excess of lithium hydroxide[ii], this method proved more effective at obtaining single phases. Further work on structures formed using this method identified that the so-called corrugated layer structure obtained by starting with γ-FeOOH, Figure 4-1, was electrochemically active[iii]. Later a new polymorph, formed by starting with the mineral goethite (α-FeOOH) was also shown to be rechargeable in a lithium cell with a cycling capacity of 0.2-0.4 $Li/LiFeO_2$ [iv]. This performance is not as good as the ramsdellite form manganese dioxide, which has a similar structure.

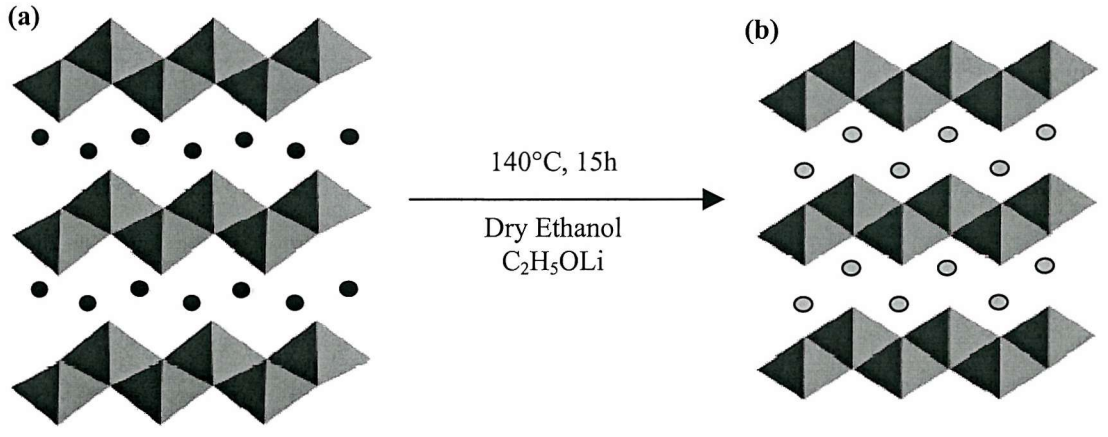

Figure 4-1: The corrugated layer form of $LiFeO_2$, the first form shown to be electrochemically active (a) Precursor γ-FeOOH (b) Ion exchange product o-$Li_{0.7}H_{0.3}FeO_2$. (Adapted from Ref. [v])

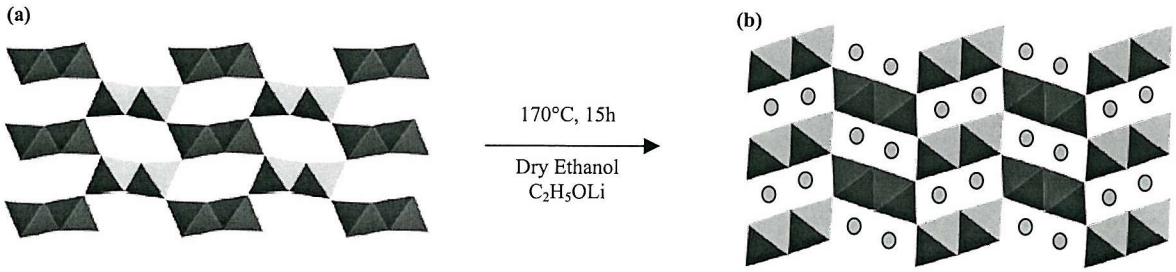

Figure 4-2: The goethite derived form of $LiFeO_2$ (a) Precursor α-FeOOH (b) Ion exchange product r-$Li_{0.8}H_{0.2}FeO_2$. Adapted from Ref. v)

The poor cyclability of these materials has been attributed to the instability of the Fe^{4+} species generated upon oxidation of the iron when lithium is de-intercalated from the structure[v], presumably due to unfavourable Jahn-Teller induced distortions. The instability of Fe^{4+} in these structures provided the impetus for our work.

This chapter outlines work on the synthesis and characterisation of $KFeO_2$[vi] and the compounds $RbFeO_2$ and $CsFeO_2$. It was hoped that these structure types, different from the layered α-$NaFeO_2$ structure, might lead to new structures of $LiFeO_2$ by exchanging the larger group 1 cations with lithium, via ion exchange reactions.

4.2 EXPERIMENTAL

It was found that the best quality samples with the highest crystalinity were obtained if dry reactants were used so all the reagent grade M_2CO_3 (M = K, Rb, Cs) and Fe_2O_3 starting materials were dried at 110°C for 48 hours and X-ray powder diffraction patterns recorded to check for phase purity.

The metal carbonate and Fe_2O_3 in a molar ratio of 1.2:1 were intimately ground in a dry nitrogen atmosphere. The mixture was pelletised at a pressure of 10 tons for 2 minutes and placed in the reaction crucible, which was covered with parafilm. The crucible was removed from the glove box and the parafilm removed just before the crucible was placed into the furnace so as to minimise exposure to moisture in the air. The mixtures were fired at 800°C for two hours, removed and reground in the glove box whilst still hot. At this point the compound had already taken on a green appearance in the case of potassium and rubidium and a dark green/black in the case of caesium. The mixtures were re-pelletised, transferred to the furnace and fired again at 800°C for 20 hrs.

X-ray analysis of the material after the first 2-hour firing indicated residual starting materials were still present. X-ray analysis after the final 20 hour firing step indicated complete conversion to a single phase.

All X-ray patterns were collected on a Bruker D8 diffractometer using a Sol-X attachment to screen out fluorescence from the iron species. A simple laboratory based analysis of these materials would have been complicated if the detector had not been available and may explain the lack of structural work on these compounds in the literature.

The moisture sensitive samples were ground and mounted on an aluminium sample holder in the glove box. A lid with a mylar window was slotted onto the sample holder and the interface sealed with vacuum grease. The seal formed was good enough to keep the sample fresh for up to the 24 hours required to obtain a good quality scan. Occasionally peaks at 2θ =38 and 44 were observed corresponding to aluminium diffraction peaks.

Rietveld analysis of the $KFeO_2$ structure was performed using powder X-ray diffraction data collected in the 2θ range 10-90° with a 0.01° step size over a 13-hour period. Neutron diffraction data for $KFeO_2$ has been published[vi] and this provided the starting model and atomic positions for the refinement. The lattice parameters from the neutron data were initially refined using the Celref program and then used in the full GSAS Rietveld refinement program[vii]. Using GSAS the lattice parameters were refined first followed by the peak profile coefficients and the atom position and thermal parameters. Zero point error was not refined; instead the peak shift parameter was varied to take into account the slight height difference of the air-sensitive sample holder compared to conventional sample holders. The refinement converged and indicated the desired structure had formed. The X-ray patterns of the rubidium and caesium compounds, for which there is no published structure for comparison, had peak positions similar to that of the potassium compound but shifted slightly to lower angles. This could indicate a possible increase in lattice parameters expected with incorporation of a larger cation into the framework.

Neutron diffraction data were collected on the rubidium and caesium samples using the POLARIS station at Rutherford Appleton Laboratories. Data from the "backscattering" C bank enabled accurate structural parameters for both samples to be obtained. In the case of the caesium compound where X-ray data alone could not distinguish between an orthorhombic or cubic space group we were able to confirm the transition to a cubic space group.

Data from the A bank of the POLARIS instrument, in the high d-spacing regime gave some insight into the magnetic structure of the samples.

4.3 RESULTS AND DISCUSSION

4.3.1 $KFeO_2$ X-Ray Structure Refinement

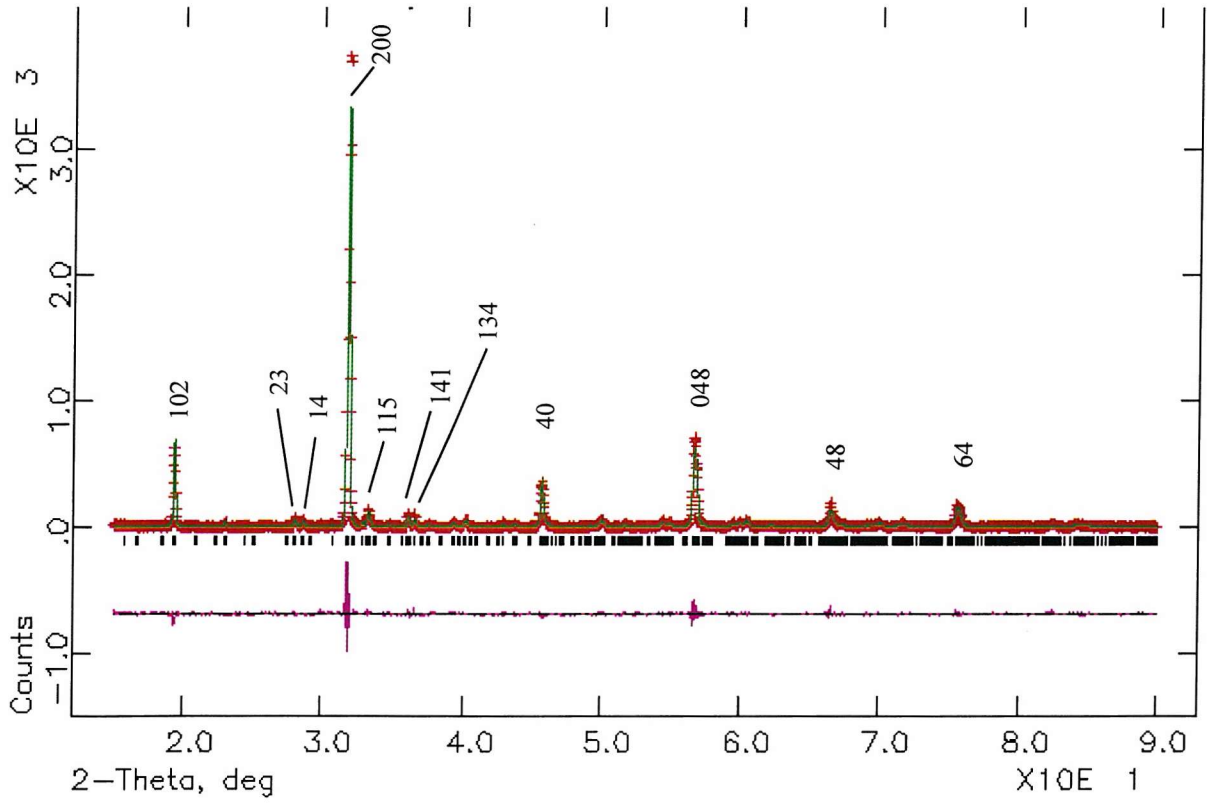

Figure 4-1: Observed (red crosses) and calculated (green line) X-ray diffraction pattern of $KFeO_2$. The purple line is the value obs-calc. R_{wp} = 21.33, χ^2 = 1.781 for 7501 observations and 40 variables.

Atom	Site	Occupancy	x	Y	z	$U_{iso}/Å^2$
K(I)	8	1	0.75036	0.010037	0.066907	4.71(36)
K(II)	8	1	0.7920(11)	0.2534(8)	0.1889(8)	1.85(26)
Fe(I)	8	1	0.2515(12)	0.0132(5)	0.1873(6)	0.73(20)
Fe(II)	8	1	0.2841(8)	0.2627(4)	0.0605(5)	0.08(17)
O(I)	1	1	0.582(4)	0.2992(18)	0.0142(10)	0.39(28)
O(II)	1	1	0.156(4)	0.4172(18)	0.0985(12)	0.39(28)
O(III)	1	1	0.3002(32)	0.1683(18)	0.1546(16)	0.39(28)
O(IV)	1	1	0.080(5)	0.4877(16)	0.2852(16)	0.39(28)

Table 4-1: Refined atomic co-ordinates for $KFeO_2$ described on Pbca. Esds are given in parentheses. *a*=5.6089(4), *b*=11.2671(9), *c*=15.9250(11).

The model used to refine the data was taken from the values obtained by neutron analysis in reference vi, the published neutron structural data and the values from the X-ray refinement above are shown below in Table 4-2.

	x		*y*		*z*	
Atom	Neutron	X-Ray	Neutron	X-Ray	Neutron	X-Ray
8K(I)	0.769(5)	0.756(1)	0.004(2)	0.010(1)	0.074(2)	0.067(0)
8K(II)	0.811(3)	0.792(11)	0.260(2)	0.253(8)	0.185(2)	0.189(8)
8Fe(I)	0.249(2)	0.252(12)	0.008(2)	0.013(5)	0.184(1)	0.187(6)
8Fe(II)	0.280(1)	0.284(8)	0.261(1)	0.263(4)	0.064(1)	0.061(5)
8O(I)	0.583(3)	0.582(4)	0.291(1)	0.299(18)	0.022(1)	0.014(10)
8O(II)	0.166(3)	0.156(4)	0.410(2)	0.417(18)	0.099(1)	0.099(12)
8O(III)	0.287(2)	0.300(32)	0.171(2)	0.168(18)	0.158(1)	0.155(11)
8O(IV)	0.089(4)	0.080(5)	0.481(1)	0.488(16)	0.282(1)	0.285(16)
	a(Å)		*b*(Å)		*c*(Å)	
	5.600(1)	5.609(4)	11.249(1)	11.267(8)	15.890(2)	15.925(11)

Table 4-2: Comparison of atomic positions and lattice parameters from neutron analysis[vi] and our X-ray analysis. Orthorhombic. Space group Pbca. Esds are given in parentheses.

4.3.2 $RbFeO_2$ X-Ray Structure Refinement

The X-ray pattern of the $RbFeO_2$ sample is very similar to that of the potassium compound therefore the same model was used to refine the structure and the initial atom positions were those of the refined $KFeO_2$ structure. Starting lattice parameters were obtained by indexing the $RbFeO_2$ X-ray pattern using Celref. The data were entered into GSAS and the three background coefficients, lattice parameters, profile coefficients and atomic positions and temperature factors were refined until the calculation converged.

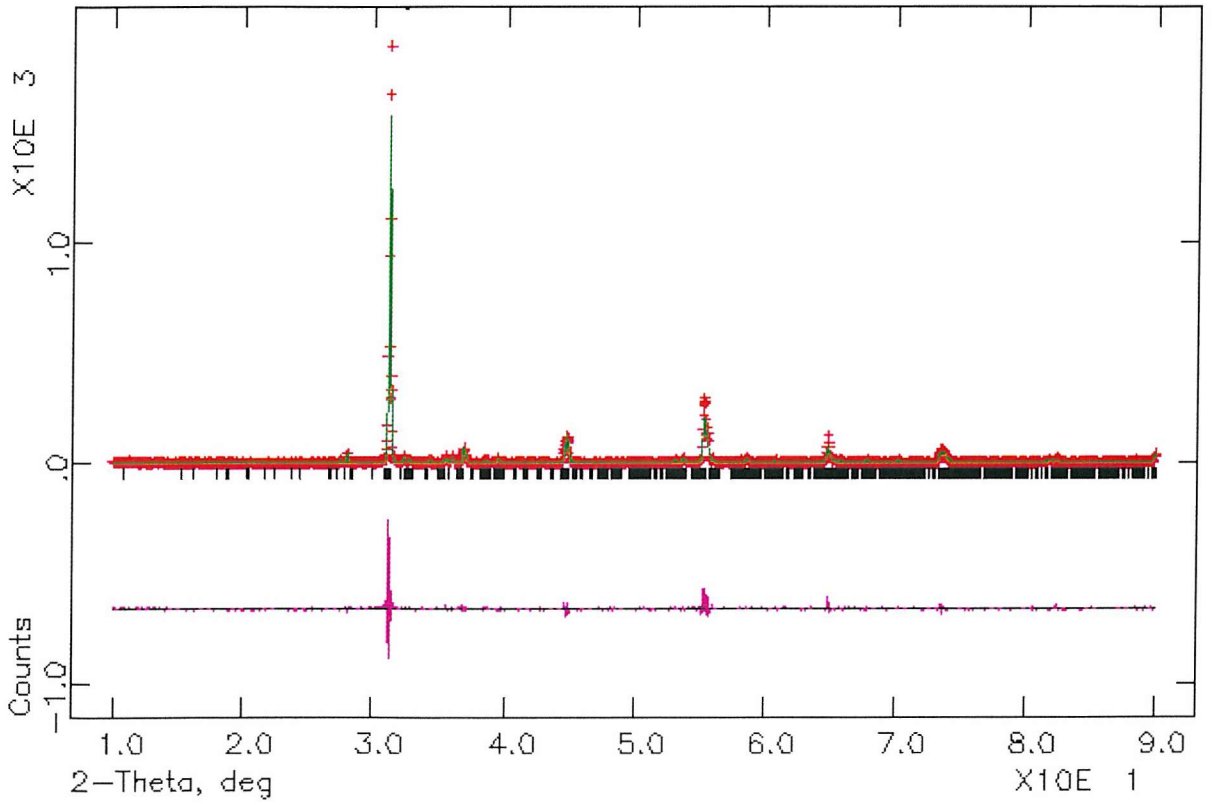

Figure 4-1: Observed (red crosses) and calculated (green line) X-ray diffraction pattern of $RbFeO_2$. The purple line is the value obs-calc. $R_{wp} = 38.81$, $\chi^2 = 1.820$ for 7999 observations and 27 variables.

Atom	Site	Occupancy	X	y	z	$U_{iso}/Å^2$
Rb(I)	8	1	0.7461(18)	0.0081(8)	0.0648(6)	2.95(32)
Rb(II)	8	1	0.7972(10)	0.2584(7)	0.1895(6)	1.05(25)
Fe(I)	8	1	0.2551(21)	0.0088(11)	0.1876(9)	-0.95(17)
Fe(II)	8	1	0.2874(13)	0.2586(13)	0.0614(9)	0.90(17)
O(I)	1	1	0.57309	0.28964	0.01922	2.5
O(II)	1	1	0.17072	0.39887	0.10722	2.5
O(III)	1	1	0.2846	0.15274	0.14913	2.5
O(IV)	1	1	0.04873	0.48	0.27609	2.5

Table 4-3: Refined atomic co-ordinates for $RbFeO_2$ described on Pbca. a=5.6089(4), b=11.2671(9), c=15.9250(11).

4.3.3 $CsFeO_2$ X-Ray Structure Refinement

Atom positions obtained from the refinement of the $RbFeO_2$ structure were used as the initial atom positions for the $CsFeO_2$ refinement.

Attempting to refine the structure using the orthorhombic space group Pbca resulted in a poor fit to the observed data. It appeared as though the distortion caused by the larger caesium cation, which was also observed but to a lesser extent in the rubidium system, was causing a transition towards a different space group. Consideration of the trend in the bond lengths and angles from the refinement indicated a move towards a cubic space group and this combined with the tetrahedrally co-ordinated iron lead us to select the cristobalite form of SiO_2 as a suitable starting model for the refinement. Starting lattice parameters were obtained by indexing the pattern using CELREF program. Using GSAS the lattice parameters, background coefficients, profile coefficients and atom temperature factors were refined until convergence was achieved. Use of the cubic space group gave a better fit than continuing with the orthorhombic model used for the potassium and rubidium compounds, Figure 4-5.

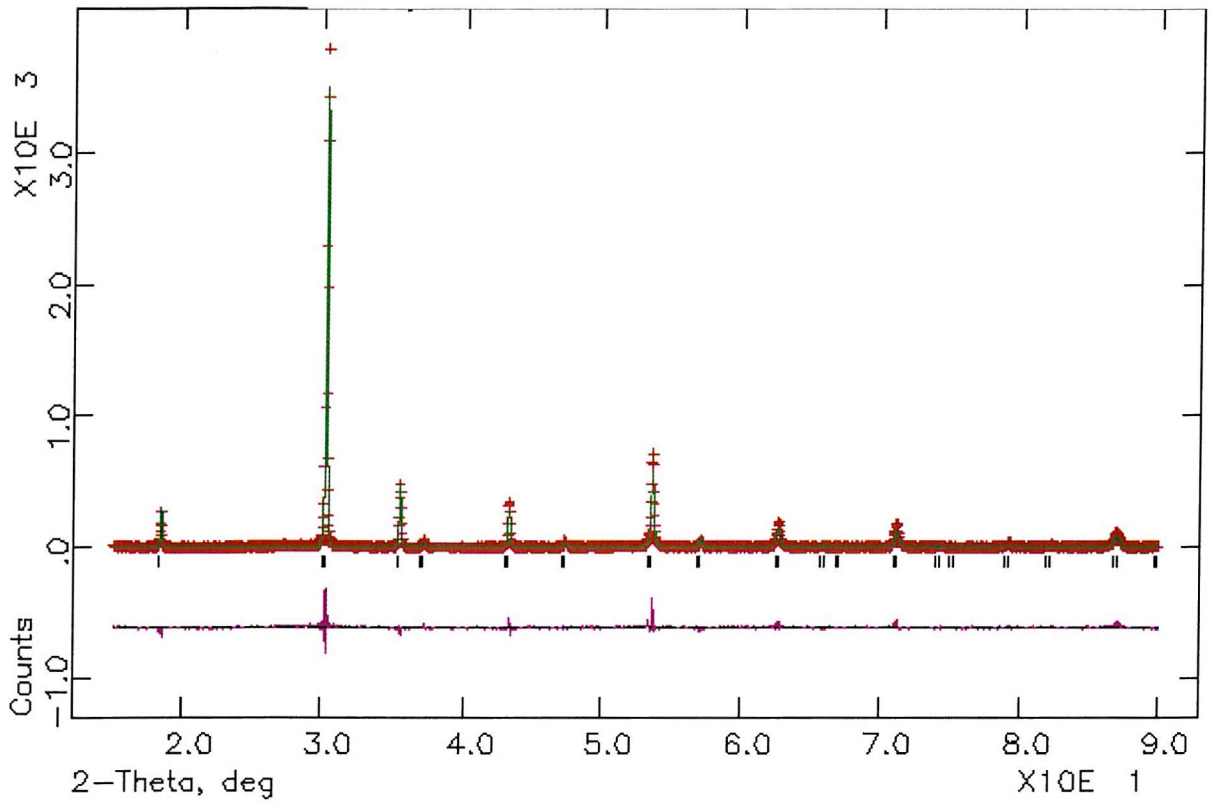

Figure 4-1: Observed (red crosses) and calculated (green line) X-ray diffraction pattern of $CsFeO_2$. The purple line is the value obs-calc. $R_{wp} = 26.21$, $\chi^2 = 2.131$ for 7398 observations and 13 variables.

Atom	Site	Multiplicity	x	y	Z	$U_{iso}/Å^2$
Cs	-43M	8	0.625	0.625	0.625	3.78
Fe	-43M	8	0.125	0.125	0.125	2.5
O	-3M(111)	16	0	0	0	5.11

Table 4-1: Refined atomic co-ordinates for $CsFeO_2$ described on Fd-3m. *a*=8.39400(29).

4.3.4 Neutron diffraction studies

X-ray analysis was not conclusive as to whether the rubidium and caesium samples adopted the orthorhombic or cubic space group suggested. The greater structural information gained from the C bank of the POLARIS instrument at Rutherford would ascertain which space group was appropriate for each system. Both samples were studied only at room temperature.

4.3.4.1 $RbFeO_2$ Neutron Diffraction studies

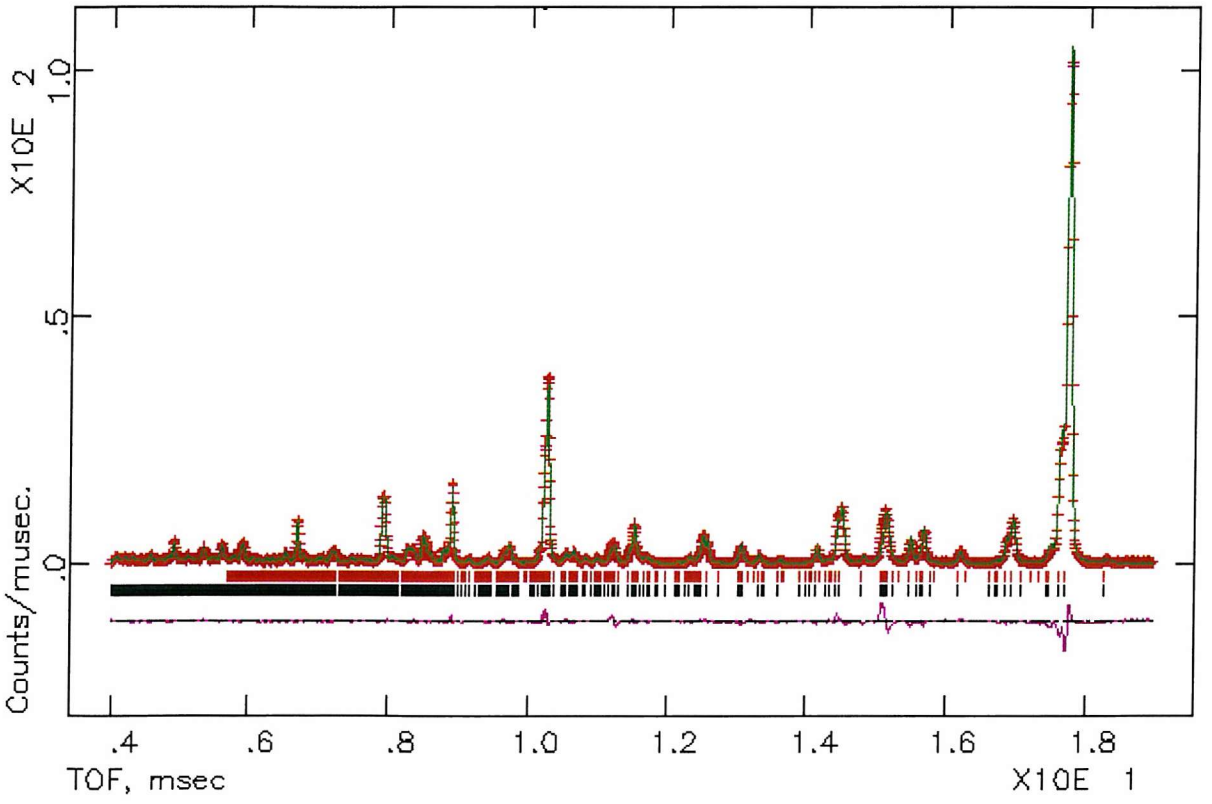

Figure 4-1: Observed (red crosses) and calculated (green line) TOF neutron diffraction pattern of $RbFeO_2$ collected from the C bank of POLARIS. The purple line is the value obs-calc. Red tick marks represent calculated magnetic unit cell reflections. Black tick marks represent structural unit cell reflections. $R_{wp} = 3.75$, $\chi^2 = 9.313$ for 3116 observations and 51 variables. Space group Pbca.

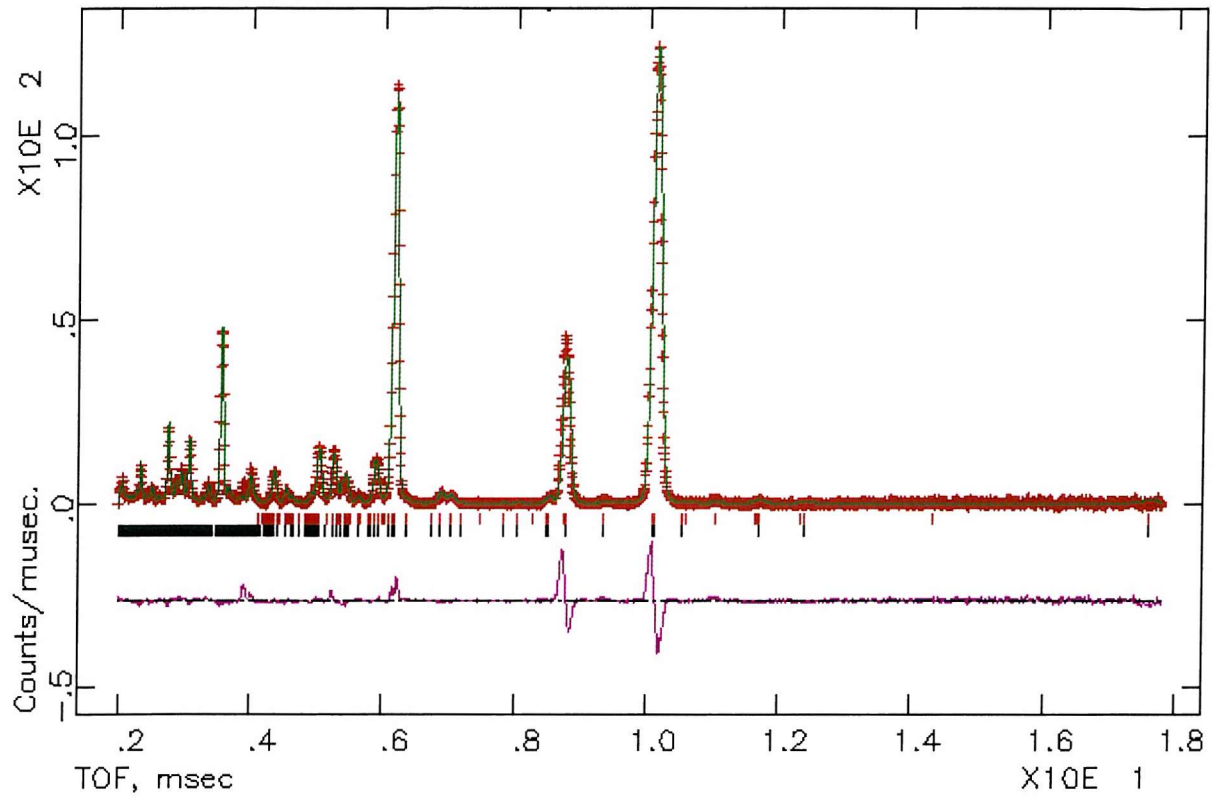

Figure 4-2: Observed (red crosses) and calculated (green line) TOF neutron diffraction pattern of $RbFeO_2$ collected from the A bank of POLARIS. The purple line is the value obs-calc. Red tick marks represent calculated magnetic unit cell reflections. Black tick marks represent structural unit cell reflections. R_{wp} = 9.50, χ^2 = 6.839 for 4370 observations and 22 variables.

Atom	Site	Occupancy	x	y	z	$U_{iso}/Å^2$
Rb(I)	8	0.7868	0.7590160(0)	0.0096250(0)	0.0621410(0)	1.15(7)
Rb(II)	8	1	0.8007(7)	0.2580(4)	0.1849(4)	1.76(8)
Fe(I)	8	1	0.2526(5)	0.00711(25)	0.18810(31)	0.90(5)
Fe(II)	8	1	0.2823(4)	0.25996(24)	0.06388(26)	0.63(5)
O(I)	1	1	0.5732(9)	0.2898(5)	0.01959(31)	1.46(11)
O(II)	1	1	0.1708(7)	0.3992(4)	0.10717(27)	0.78(8)
O(III)	1	1	0.2848620(0)	0.1527370(0)	0.1491310(0)	2.59(12)
O(IV)	1	1	0.0516(9)	0.4777(6)	0.2756(4)	2.20(11)

Table 4-1: $RbFeO_2$ atomic coordinates obtained from fitting the POLARIS C bank data. Space group Pbca. *a*=5.71692(19) *b*=11.5029 *c*=16.3048(6).

4.3.4.2 *$CsFeO_2$ Neutron Diffraction studies*

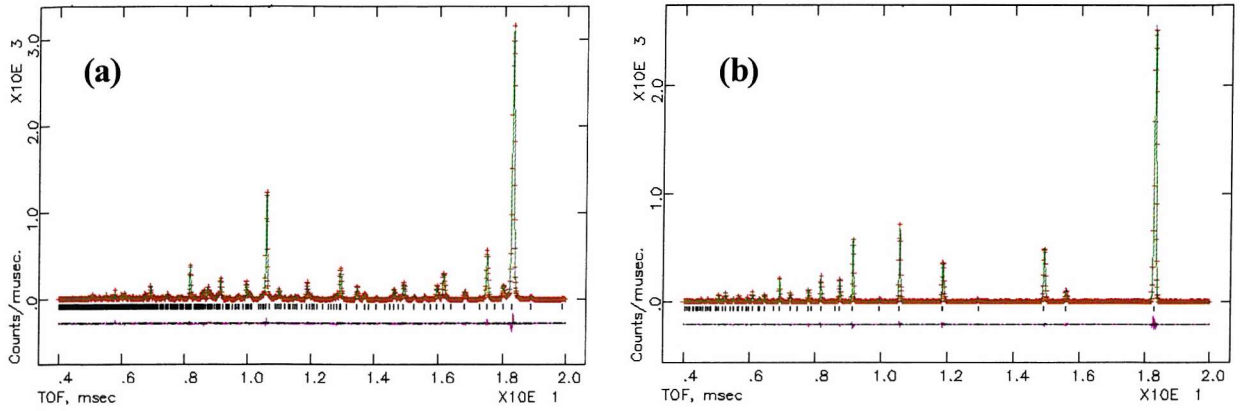

Figure 4-1: Dummy histograms of $CsFeO_2$ modelled in (a) orthorhombic and (b) cubic system

The fit presented in Figure 4-2 confirms that, of the two possibilities presented in Figure 4-1, the cubic space group should be used to model the system.

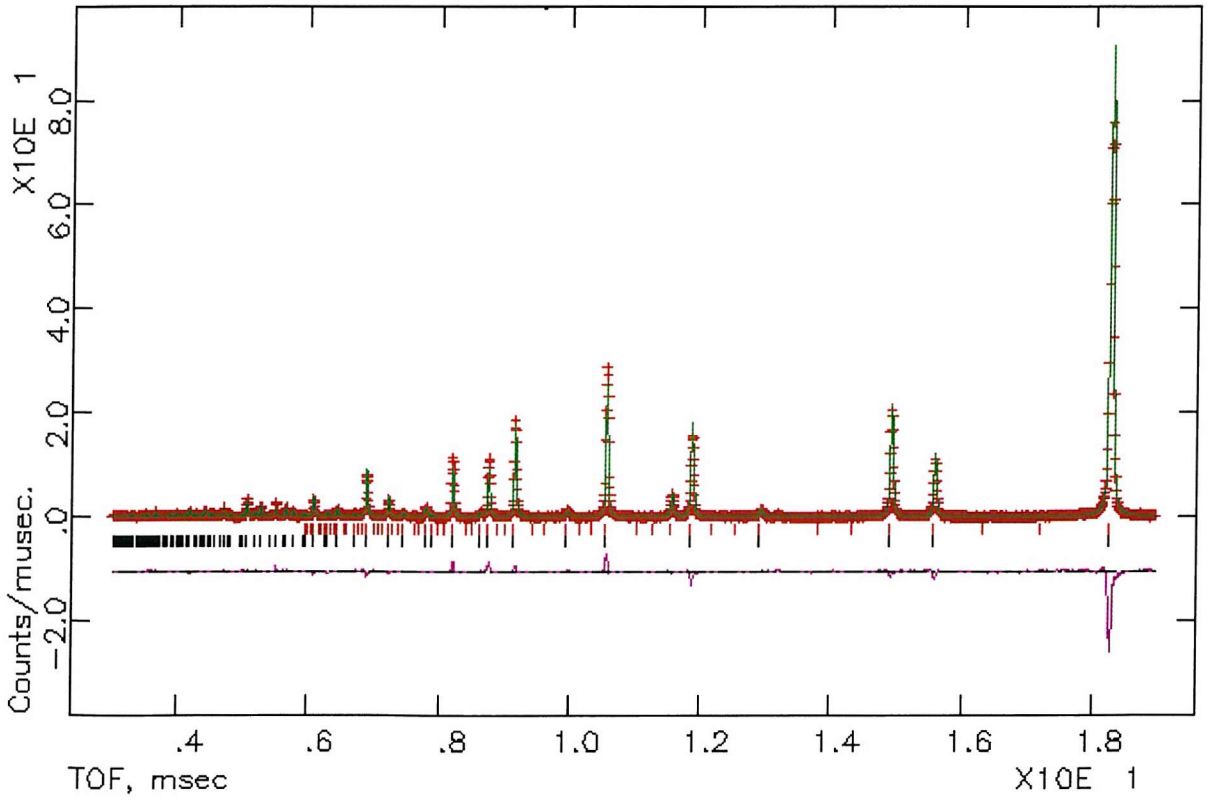

Figure 4-2: Observed (red crosses) and calculated (green line) TOF neutron diffraction pattern of $CsFeO_2$ collected from the C bank of POLARIS. The purple line is the value obs-calc. Red tick marks represent calculated magnetic unit cell reflections. Black tick marks represent structural unit cell reflections. R_{wp} = 4.82, χ^2 = 14.44 for 3692 observations and 23 variables.

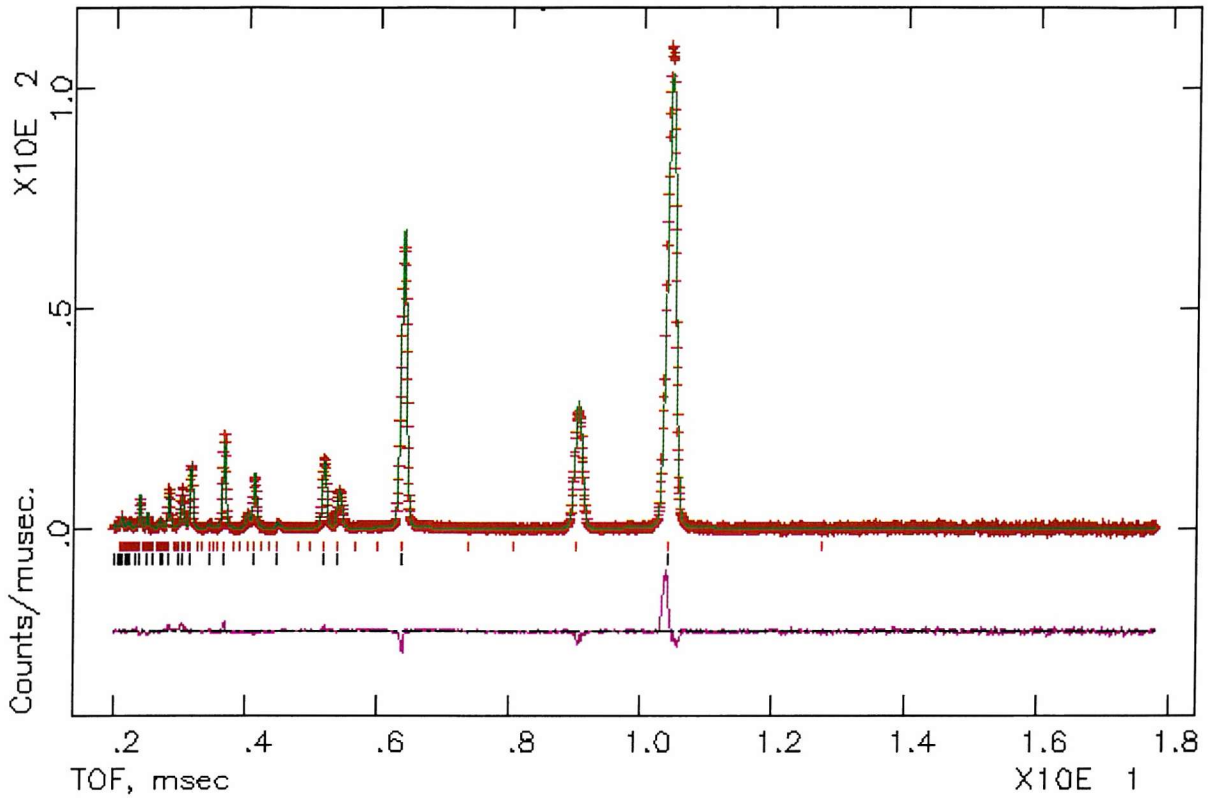

Figure 4-3: Observed (red crosses) and calculated (green line) TOF neutron diffraction pattern of $CsFeO_2$ collected from the A bank of POLARIS. The purple line is the value obs-calc. Red tick marks represent calculated magnetic unit cell reflections. Black tick marks represent structural unit cell reflections. R_{wp} = 6.68, χ^2 = 2.387 for 4370 observations and 20 variables.

Atom	Site Occupancy	x	y	z	$U_{iso}/Å^2$
Cs	0.804(13)	0.625	0.625	0.625	3.32(9)
Fe	1	0.125	0.125	0.125	1.112(23)
O	1	0	0	0	6.79(9)

Table 4-1: Atomic coordinates of $CsFeO_2$ obtained from fitting the POLARIS C bank data. *a*=8.38480(8). Space group Fd-3m.

4.3.5 Interatomic Distances and Bond Angles from Neutron Studies

$KFeO_2$

Fe(I)-O	Fe(II)-O	K(I)-O	K(II)-O	Fe-K	Fe(I)-O(III)-Fe(II)
1.81	1.86	3.50	2.91	3.21	136.1° [2×]
1.90	1.86	3.56	3.13	3.25	**Fe(I)-O(II)-Fe(II)**
1.82	1.88	2.66	2.69		132.7° [2×]
1.99	1.80	2.69	2.84		**Fe(I)-O(IV)-Fe(I)**
K-K		2.44	2.95		132.8° [2×]
3.38		3.28	2.87		**Fe(II)-O(I)-Fe(II)**
3.29		2.98	3.32		138.9° [2×]
3.50		3.36	3.23		
3.48 [2×]					

$RbFeO_2$

Fe(I)-O	Fe(II)-O	Rb(I)-O	Rb(II)-O	Fe-Rb	Fe(I)-O(III)-Fe(II)
1.864(6)	1.845(5)	3.463(5)	3.016(8)	3.3563(33)	151.69° [2×]
1.801(4)	1.900(7)	2.792(5)	3.721(8)	3.874(5)	**Fe(I)-O(II)-Fe(II)**
1.845(8)	1.862(6)	3.213(5)	2.953(7)		139.50° [2×]
1.868(6)	1.858(4)	2.862(4)	3.831(8)		**Fe(I)-O(IV)-Fe(I)**
Rb-Rb		3.575(4)	3.077(4)		141.0° [2×]
3.59528(9)		2.996(5)	3.241(4)		**Fe(II)-O(I)-Fe(II)**
3.42744(8)		3.70932(9)	2.966(6)		142.34° [2×]
3.497(5)		3.47413(8)	3.260(8)		
3.536(5)					

$CsFeO_2$

Fe-O	Cs(I)-O	Cs(II)-O	Fe-Cs	O-Fe-O
1.81536(1)	3.47615(3)	3.47616	3.63073(3)	109.471(0)
Cs-Cs			4.19240(4)	**Fe-O-Fe**
3.63073				179.972(0)

Table 4-7: Selected interatomic bonds distances and angles from neutron studies. The values for $KFeO_2$ are taken from ref. vi.

4.3.6 Crystal structure diagrams

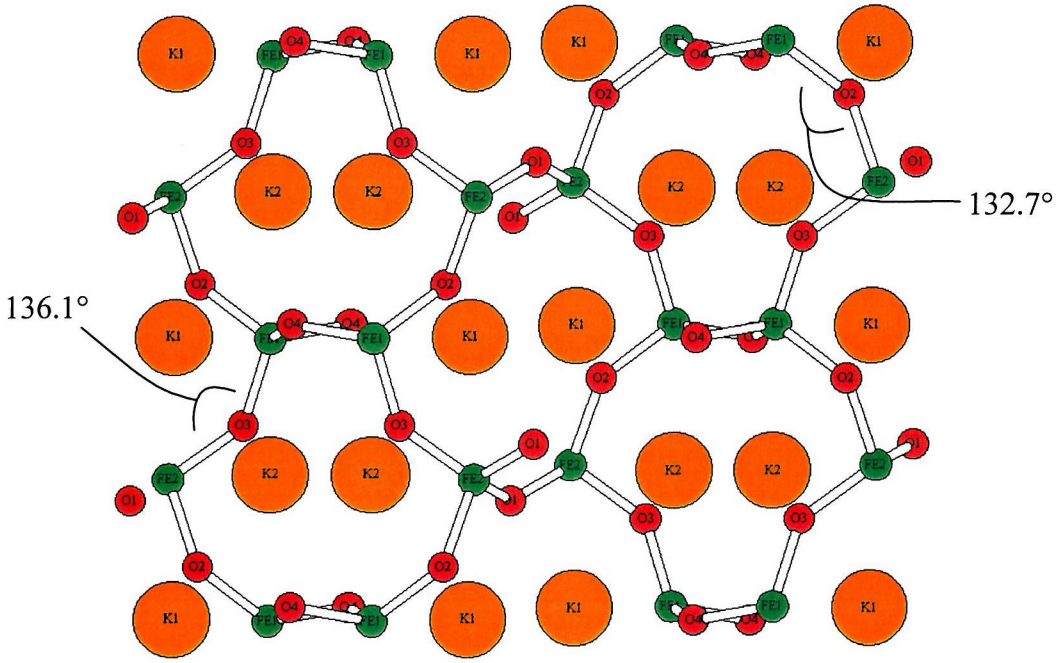

Figure 4-1: The crystal structure of $KFeO_2$ viewed down the a axis

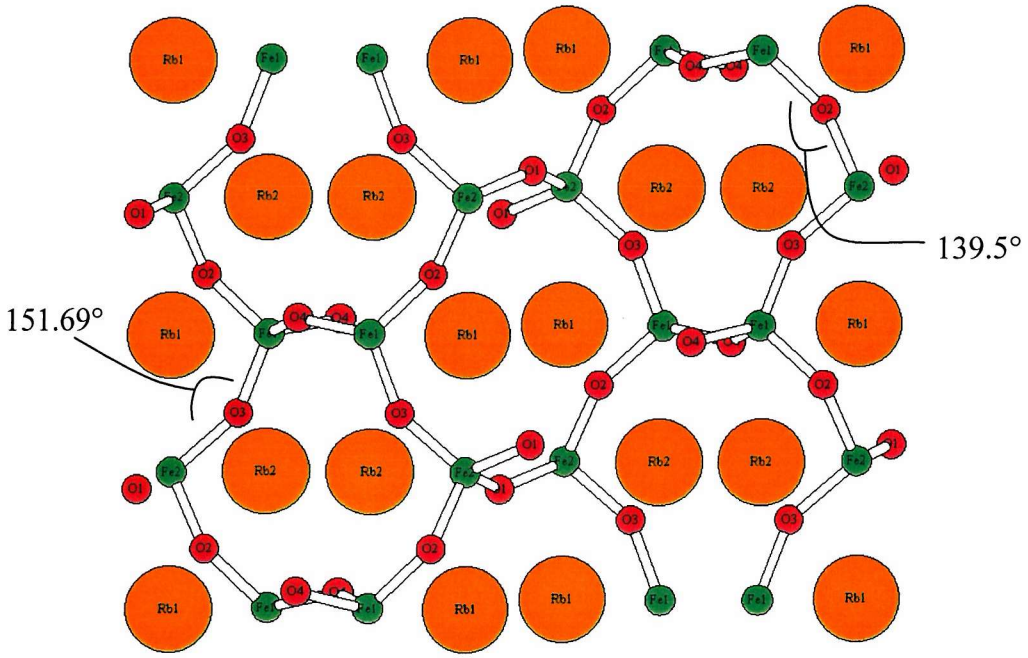

Figure 4-2: The crystal structure of $RbFeO_2$ viewed down the a axis

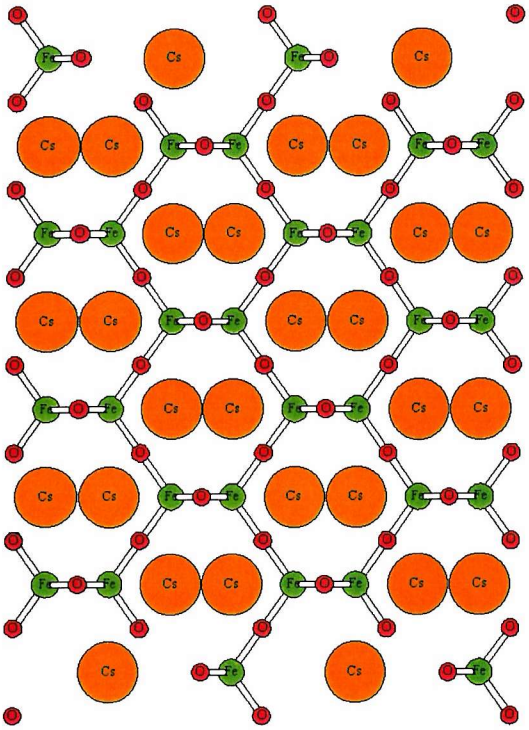

Figure 4-3: The crystal structure of $CsFeO_2$ viewed down the a axis

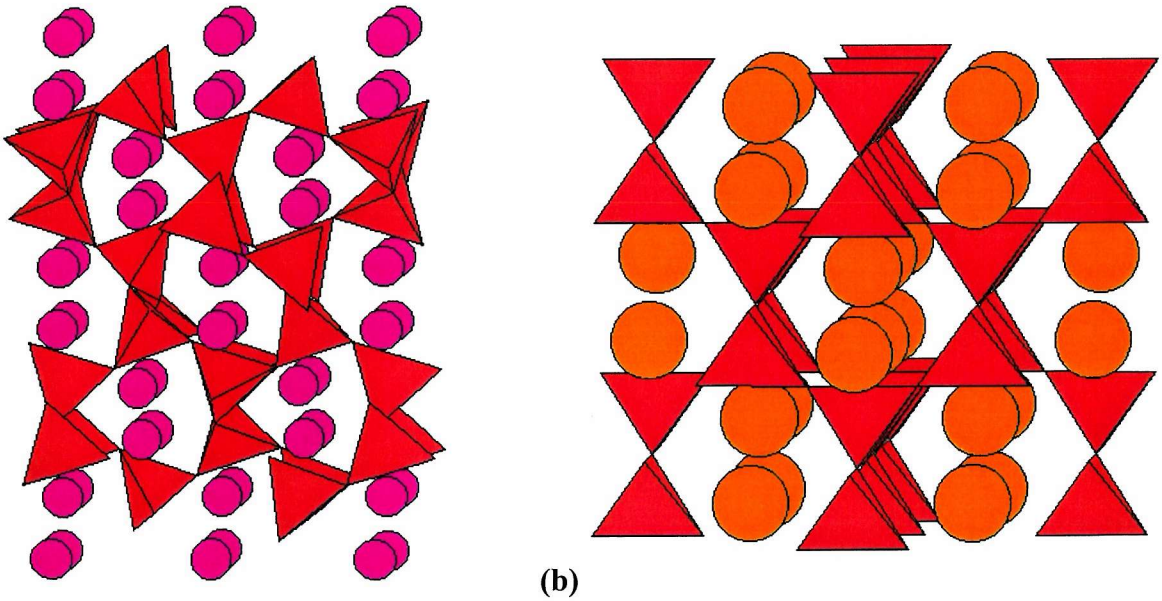

(a) **(b)**

Figure 4-4: An alternative view of the structures of (a) $RbFeO_2$ and (b) $CsFeO_2$ showing the channels between the iron tetrahedra

4.4 ION EXCHANGE REACTIONS

The 6 membered ring channels in the group 1 ferrites suggest that the alkali ion in the framework may be exchangeable. Attempts were made to exchange the potassium ion in $KFeO_2$ with lithium by both *chimie-douce* and solvothermal methods.

4.4.1 The chimie-douce method

The *chimie-douce* reaction has been used increasingly as a method for performing ion exchanges in relatively mild conditions, generally with intercalation compounds[viii,ix,x]. It was hoped that the method, using a low temperature and anhydrous solvents, would avoid the brake-up of the tetrahedrally co-ordinated iron framework.

$KFeO_2$, lithium bromide and 18-crown-6 were combined, in a 1:20:6 ratio, in a Schlenk tube. The crown ether was used to complex any potassium released from the $KFeO_2$ in the reaction. The starting materials were dissolved in anhydrous ethanol in a Schlenk tube and the solution was refluxed under nitrogen for periods of 2 to 12 hours. The resulting green or brown solid was filtered and residual solvent removed under vacuum. Green solids, obtained with short refluxing times or temperatures of around 70°C, were found to be the starting $KFeO_2$. A brown product, the result of longer refluxing periods or higher (80°C) temperatures, was X-rayed and found to be a mixture of products but mainly Fe_2O_3 indicating collapse of the tetrahedrally co-ordinated iron structure to its more familiar octahedral environment.

The reaction was also attempted using the higher temperatures possible with anhydrous hexanol as the solvent. The result was again either no reaction at all, with recovery of the starting material, or under more vigorous conditions, collapse of the structure.

4.4.2 Solvothermal Bomb Ion-Exchange

An alternative method of trying to force the material to undergo ion exchange was to apply pressure as well as elevated temperature. This could be achieved using a bomb with a Teflon liner.

The starting materials $KFeO_2$, $LiNO_3$ and 18-crown-6 in the ratio 1:20:6 were placed in a 23ml Teflon liner with 10ml of anhydrous ethanol, under a nitrogen atmosphere. The bomb was sealed and placed in an oven at 70°C for 4 days. The green product was washed with petroleum ether 40/60 and dried under vacuum. X-ray analysis showed starting material was present but also

some KNO_3. The only source of potassium was the $KFeO_2$ therefore this result indicated some potassium ions had been leached from the compound. The analysis did not contain any other peaks.

4.4.2.1 EDAX analysis

EDAX analysis provided a crude method of comparing the ratios of potassium to iron and oxygen in the sample before and after the solvothermal ion exchange, the results are presented in Table 4-8.

Non-Ion Exchanged Sample

Element	Wt %	At %	Net Integral	Integral Error
O K	17.93	39.3	87.75	1.14
K K	34	30.5	137.61	0.92
FeK	48.07	30.19	23.7	2.31
Total	100	100		

Sample Following Ion Exchange

Element	Wt %	At %	Net Integral	Integral Error
O K	20.83	44.34	98.63	1.37
K K	28.28	24.63	100.61	1.37
FeK	50.89	31.03	22.09	2.93
Total	100	100		

Table 4-8: Area scans of a sample before and after solvothermal ion exchange. Ion exchange sample was washed with petroleum ether and X-rayed to ensure removal of KNO_3. (×130 magnification)

Typical errors associated with elemental analysis by EDAX are of the order of 1-2% therefore whilst the EDAX evidence is obviously not conclusive the results do give an indication that it may be possible to extract potassium from the framework. It is not possible to detect lithium, with its small number of electrons, using the EDAX technique therefore it is impossible to say if lithium has replaced potassium in the structure. Future work should use a longer reaction time for the ion-exchange reaction, for example 15 days is used when starting with FeOOH, Figure 4-1, to give the kinetically slow reaction time to proceed.

Neutron analysis, if flame photometry and EDAX results proved encouraging in terms of potassium content, would establish whether lithium had exchanged into the structure.

4.5 CONCLUSIONS

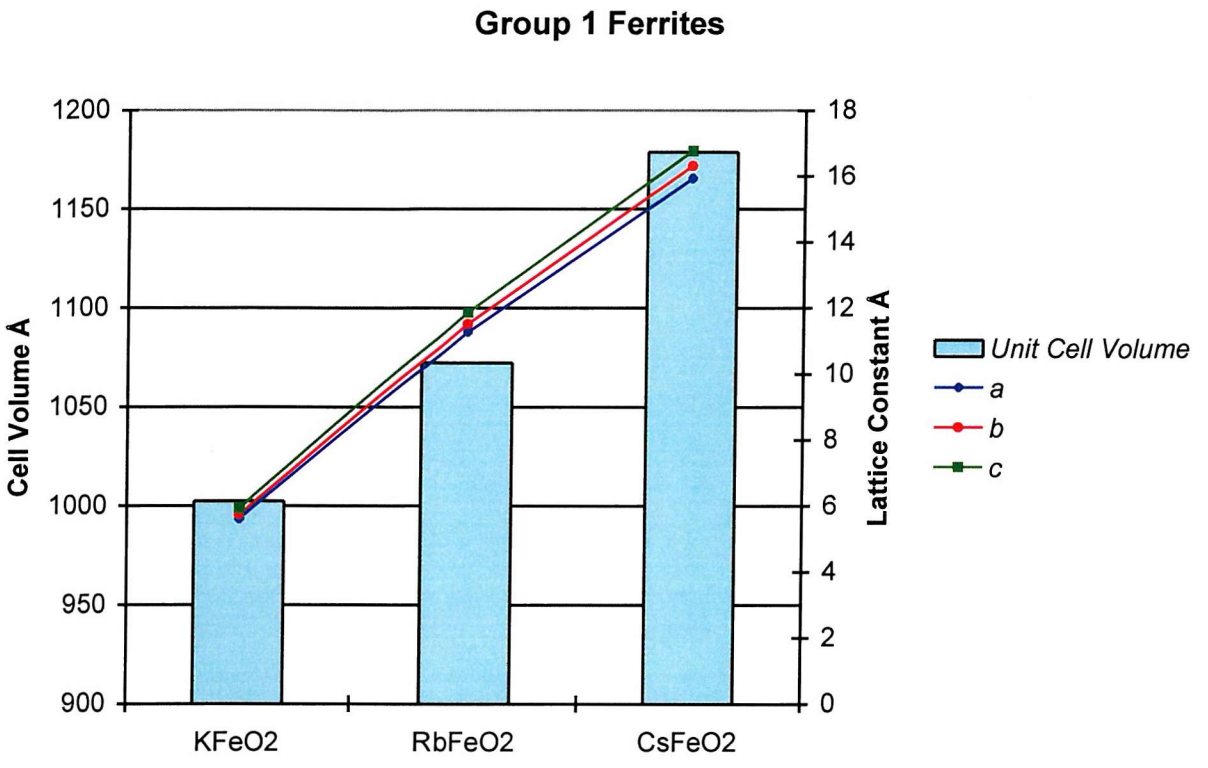

Figure 4-1: The variation in unit cell volume (left axis) and lattice parameter (right axis) in the group 1 ferrites, $CsFeO_2$ converted to pseudo-orthorhombic.

This work has, for the first time, investigated the structure of the two group 1 iron oxides $RbFeO_2$ and $CsFeO_2$. The expected increase in lattice parameter has been observed as the ionic radii of the alkali cation in the iron-oxygen channels is increased, Figure 4-1. In addition it has been shown that the distortion caused to the structure by the incorporation of larger cations causes a transition from an orthorhombic crystal structure, adopted by $KFeO_2$, to a cubic crystal structure adopted by $CsFeO_2$. This change has been confirmed by neutron diffraction analysis, which also revealed that the rubidium and caesium structures are deficient in their respective group 1 cation.

These materials have been investigated in terms of their utility as solid electrolytes when prepared as a solid solution of the type $(A_{1-x}A'_xFeO_2)\cdot 0.25EO_2$ (A, A' = K, Rb, Cs; E=Si, Ti, Ge)[xi]. The discovery that the pure compounds are alkali cation deficient means that investigation of their ionic conductivity would be worthwhile.

The results of the solvothermal ion exchange and subsequent EDAX analysis also tentatively suggest that the alkali cations may be labile in the channels created by the iron-oxygen tetrahedra, again providing impetus for further investigation of their ionic conductivity. This result also suggests that it may indeed be able to synthesise a new form of $LiFeO_2$ given a longer reaction time.

Magnetic peaks were observed in the neutron diffraction patterns of the rubidium and caesium compounds. The variation in the iron tetrahedra bond angles and lengths with the cation will affect the size of the interaction between the magnetic moments of the iron ions. It would be interesting therefore to measure the magnetic moments of the samples and correlate this to the change in the structural characteristics of the molecule.

Further investigation of the structural transition could be carried out by preparing a range of solid solutions with the formula $Rb_xCs_{1-x}FeO_2$ (x=0.2, 0.4, 0.6, 0.8) and then analysing the peak positions of the X-Ray diffraction patterns. This may reveal a critical composition where the transition to the cubic space group occurs.

4.6 REFERENCES

[i] Shirane T, Kanno R, Kawamoto Y, Takeda Y, Takano M, Kamiyama T, Izumi F, *Solid State Ionics*, **79**, 227-233, (1995)

[ii] Tabuchi M, Ado K, Sakaebe H, Masquelier C, Kageyama H, Nakamura O, *Solid State Ionics*, **79**, 220-226, (1995)

[iii] Kanno R, Shirane T, Kawamoto Y, Takeda Y, Takano M, Ohashi M, Yamaguchi Y, *J. Electrochem. Soc.*, **143**, 2435, (1996)

[iv] Sakurai Y, Arai H, Okada S, Yamaki J, *Jnl Power Sources*, **68**, 711-715, (1997)

[v] Bordet-Le Guenne L, Deniard P, Lecerf A, Biensan P, Siret C, Fournes L, Brec R, *J. Mat. Chem*, **9**, 1127-1134, (1999)

[vi] Tomkowicz Z, Szytula A, *Phys. Chem. Solids*, **38**, 1117 (1977)

[vii] Larson AC, Von Dreele RB, General Structural Analysis System, 1986 LAUR86-748

[viii] Armstrong AR, Bruce PG, *Nature*, **381**, 499 (1996)

[ix] Armstrong AR, Robertson AD, Gitzendanner R, Bruce PG, *J. Solid State Chem.*, **145**, 549, (1999)

[x] Raekelboom EA, *SU Thesis*, (2001)

[xi] Smirnov NB, Burmakin EI, Shekhtman GS, *Russ. Jnl. Elec.* **32**, 5, 514-517, (1996)

5 High Pressure Routes to Manganese Materials

5.1 INTRODUCTION

The general trend within this project work has been the drive towards the stabilisation of unusually high oxidation states for particular transition metal ions. In order to achieve these "unusual" oxidation states it may be necessary to utilise "unusual" reaction conditions. The specialised high pressure apparatus described in the experimental chapter allows hydrothermal and solid state reactions to be carried out at elevated pressure and temperature, leading hopefully to many more possibilities for new reaction conditions and therefore products.

Of particular interest when studying battery materials are sheet-like structures, which allow for the reversible intercalation of lithium ions with minimal disruption to the structure. We have already seen in the introductory chapter how manganese alternatives to the cobalt system are desirable in terms of cost, weight and toxicity. Bruce has achieved layered $LiMnO_2$ via ion-exchange from α-$NaMnO_2$[i] but the cyclability of such materials is poor due to the continual oxidation and reduction from and to the Jahn-Teller active Mn^{3+} ion. Doping with cobalt alleviates the problems somewhat but also is counterproductive as the main aim is to move away from the need for cobalt.

Chang and Jansen utilised high pressures and temperatures to synthesise $Na_2Mn_3O_7$[ii], a compound made up of $Mn_3O_7^{2-}$ layers separated by interlamellar sodium ions. Raekelboom et al then converted this, through a *chemie-douce* ion exchange reaction to $Li_2Mn_3O_7$[iii]. $Li_2Mn_3O_7$ is suitable for use in a lithium cell and has the advantage of being based on Mn(IV) rather than Mn(III). After the first complete discharge stage the structure stoichiometry is effectively $LiMn_{0.86}O_2$ as one and a half lithium ions are intercalated into the structure. Even at the end of this stage, only 50% of the manganese ions are in the +3 oxidation state, which keeps Jahn-Teller induced structural distortions to a minimum.

The aim of our work was to use high-pressure techniques to try and synthesise the potassium analogue of the sodium compound, the material $K_2Mn_3O_7$, and investigate how its structure differed from that of the sodium analogue. If successful then we would also investigate whether subsequent ion-exchange of potassium with lithium offered any potential new battery materials.

5.2 EXPERIMENTAL

5.2.1 $Na_2Mn_3O_7$

To gain practice with the equipment the synthesis of $Na_2Mn_3O_7$, as performed by Raekelboom, was repeated[iii]. The starting oxides, MnO_2 and Na_2O, were both dried at 110°C for 48hrs. Stoichiometric amounts of the oxides were then ground together in the glove box and poured carefully into a 2.5cm length piece of gold tubing which had previously been welded shut at one end. Once the sample was loaded the other end of the tube was pinched shut and the end cut to give a smooth edge. The capsule was then removed from the glove box and quickly welded shut to complete the seal. The capsule was placed into a high-pressure bomb, attached to the rig and then heated to 600°C under 1.4kBar for 2 days. The dark grey powder product was ground in the glove box and X-rayed on a Siemens D5000 diffractometer, Figure 5-1.

The pattern matches that reported by Raekelboom for $Na_2Mn_3O_7$ indicating that the desired phase has formed.

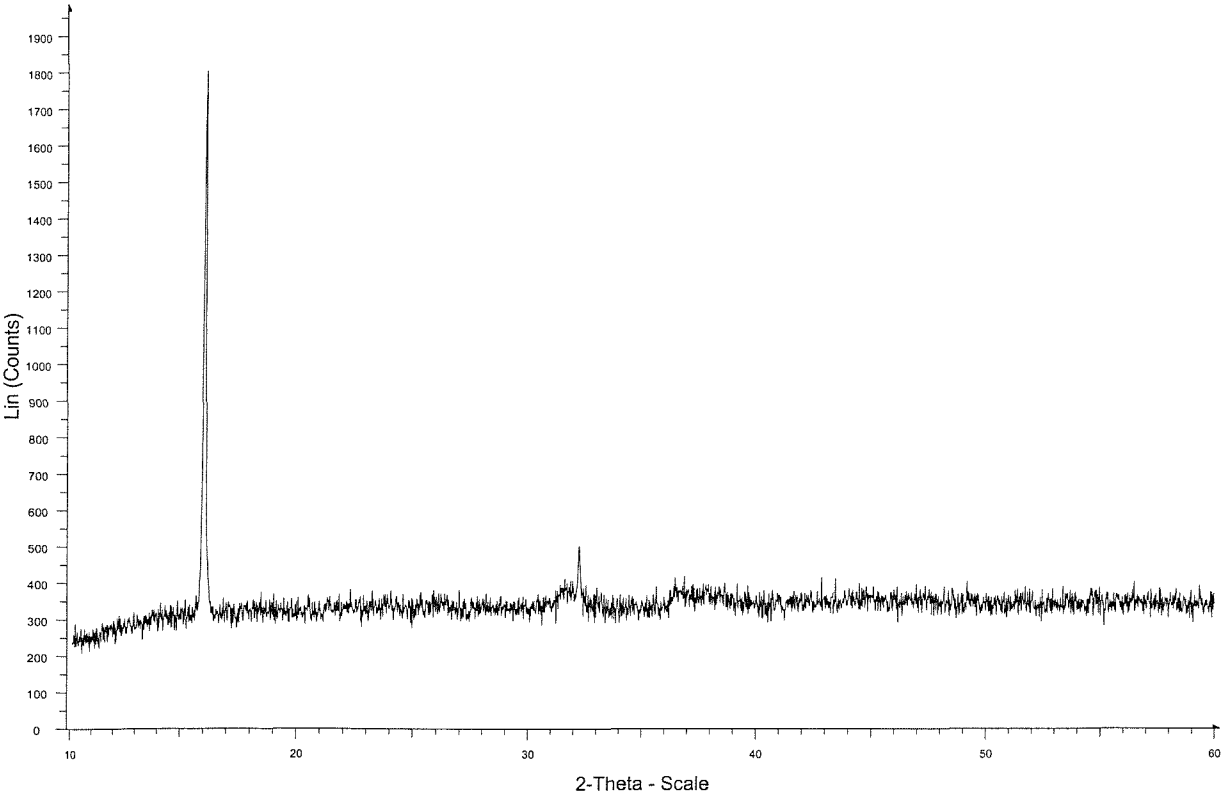

Figure 5-1: The XRD pattern of $Na_2Mn_3O_7$

5.2.2 $K_2Mn_3O_7$

The synthesis of $Na_2Mn_3O_7$ uses the oxide Na_2O as a starting material. The equivalent potassium oxide cannot be obtained therefore potassium superoxide, KO_2 was used.

This complicated the choice of a suitable starting stoichiometry for the synthesis of $K_2Mn_3O_7$ as every combination of +3/+4 manganese oxides and potassium superoxide gave excess oxygen. The closest combination of suitable starting materials was;

$$2KO_2 + 2MnO_2 + MnO \rightarrow K_2Mn_3O_7 + O_2.$$

The dried starting materials were ground in the glove box and sealed into a gold bomb. The bomb was heated to 400°C and pressurised to 3.1kBar for 24hrs.

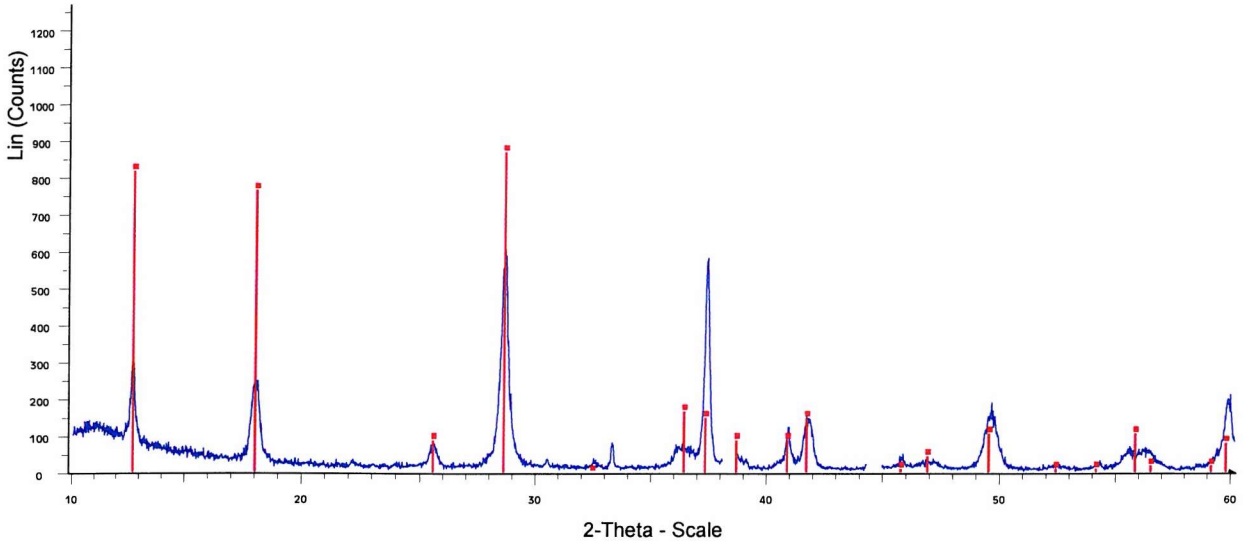

Figure 5-1: XRD pattern of reaction product (blue line) suggesting $K_{1.33}Mn_8O_{16}$ (red peaks) has formed in preference to the desired phase $K_2Mn_3O_7$.

The $K_{1.33}Mn_8O_{16}$ formed in the reaction above is a mixed-valent Mn(III)/Mn(IV) compound. A second attempt at synthesising $K_2Mn_3O_7$ used only MnO_2 to try and force the manganese to adopt its +4 oxidation state in the structure. KO_2 and MnO_2 were ground together in stoichiometric amounts and heated in a gold bomb at 400°C and a pressure of 2.75kBar for 2 days. The XRD pattern of the product, Figure 5-2, indicated that K_2MnO_4 had formed.

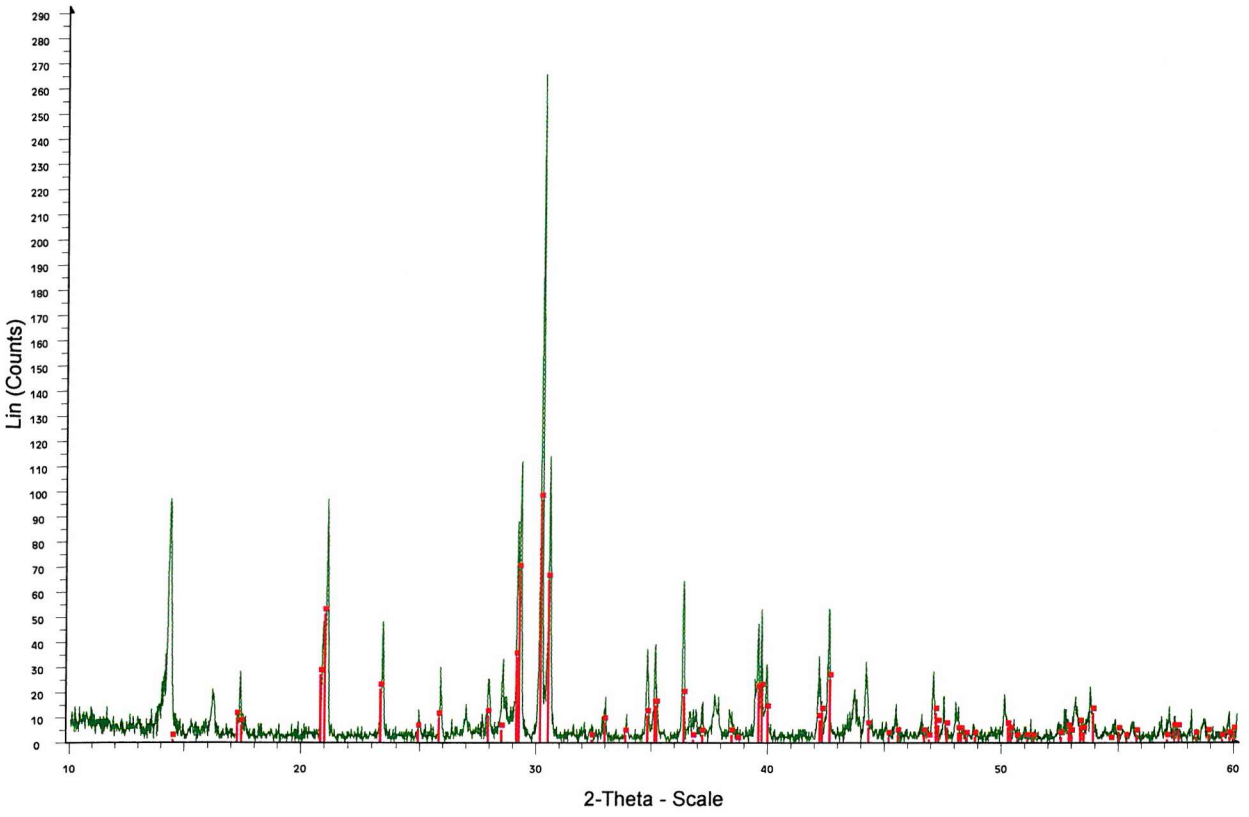

Figure 5-2: XRD pattern (green line) of the product of the reaction between KO_2 and MnO_2 (400°C, 2.75kBar, 2days). The diffraction pattern of K_2MnO_4 is superimposed (red line)

5.3 DISCUSSION

It appears from our initial results as though the potassium analogue of the layered $Na_2Mn_3O_7$ does not form under the same reaction conditions and with the closest available equivalent starting materials.

The attempted synthetic route actually resulted in the formation of $K_{1.33}Mn_8O_{16}$ or possibly MnO_2. The material $K_{1.33}Mn_8O_{16}$ is mixed valence Mn^{3+}/Mn^{4+} a property that we have already seen helps reduce the effect of Jahn-Teller distortions upon the structure. The hollandite structure contains large channels and pores suitable for ion diffusion and may therefore hold potential as battery materials. This should be investigated in future work.

The use of only MnO_2 along with potassium superoxide as the starting materials failed to prevent the formation of the mixed valent compound.

5.4 REFERENCES

[i] Armstrong AR, Bruce PG, *Nature*, **381**, 499, (1996)

[ii] Chang J, Jansen M, *Anorg. Allg. Chem.*, **531**, 177 (1985)

[iii] Raekelboom EA, Hector AL, Owen J, Vitins G, Weller MT, *Chem. Mater.* **13**, (12), 4618, (2001)